JGR Space Physics

RESEARCH ARTICLE
10.1029/2023JA031468

Non-Migrating Structures in the Northern Midlatitude Thermosphere During December Solstice Using ICON/MIGHTI and FPI Observations

L. A. Navarro[1,2], J. J. Makela[1], J. M. Forbes[3], B. J. Harding[4], C. R. Englert[5], J. M. Harlander[6], K. D. Marr[5], R. Kerr[7], J. Noto[7], Q. Wu[8], Z. Benkhaldoun[9], M. Kaab[9], and T. J. Immel[4]

[1]Department of Electrical and Computer Engineering, University of Illinois Urbana-Champaign, Urbana, IL, USA, [2]Space Weather and Technology, Research, and Education Center, University of Colorado, Boulder, CO, USA, [3]Ann and H. J. Smead Department of Aerospace Engineering Sciences, University of Colorado, Boulder, CO, USA, [4]Space Sciences Laboratory, University of California, Berkeley, Berkeley, CA, USA, [5]Space Science Division, US Naval Research Laboratory, Washington, DC, USA, [6]Space Systems Research Corporation, Alexandria, VA, USA, [7]Computational Physics, Inc., Lowell, MA, USA, [8]National Center for Atmospheric Research, High Altitude Observatory, Boulder, CO, USA, [9]Oukaimeden Observatory, Laboratoire de Physique des Hautes Energies et Astrophysique, FSSM, Cadi Ayyad University, Marrakech, Morocco

Key Points:

- Persistent nighttime structures in thermospheric winds during the 2019 December solstice are interpreted to have tidal origin
- Strong non-migrating tides are observed in coincident and historical midlatitude thermospheric winds from different observing platforms
- Latitude-longitude dependence of wind structure tends to follow magnetic field topology, and tidal signatures migrate from lower latitudes

Correspondence to:
L. A. Navarro,
luis.navarro@colorado.edu

Citation:
Navarro, L. A., Makela, J. J., Forbes, J. M., Harding, B. J., Englert, C. R., Harlander, J. M., et al. (2023). Non-migrating structures in the northern midlatitude thermosphere during December solstice using ICON/MIGHTI and FPI observations. *Journal of Geophysical Research: Space Physics*, *128*, e2023JA031468. https://doi.org/10.1029/2023JA031468

Received 8 MAR 2023
Accepted 25 AUG 2023

Abstract Midlatitude thermospheric wind observations from the Michelson Interferometer for Global High-resolution Thermospheric Imaging on board the Ionospheric Connections Explorer (ICON/MIGHTI) and from the ground-based Boulder, Urbana, Millstone Hill and Morocco Fabry-Perot interferometers (FPIs) are used to study a distinct solar local time (SLT) evolution in the nighttime wind field around the December solstice period. Our results show, to the best of our knowledge for the first time, strong non-migrating tides in midlatitude thermospheric winds using coincident from different observing platforms. These observations exhibited a structure of strong (~50–150 m/s) eastward and southward winds in the pre-midnight sector (20:00–23:00 SLT) and in the post-midnight sector (02:00–03:00 SLT), with a strong suppression around midnight. Tidal analysis of ICON/MIGHTI data revealed that the signature before midnight was driven by diurnal (D0, DE1, DE2, DW2) and semidiurnal (SE2, SE3, SW1, SW4) tides, and that strong terdiurnal (TE2, TW1, TW2, TW5) and quatradiurnal (QW2, QW3, QW6) tides were important contributors in the mid- and post-midnight sectors. ICON/MIGHTI tidal reconstructions successfully reproduced the salient structures observed by the FPI and showed a longitudinal dual-peak variation with peak magnitudes around 200°–120°W and 30°W–60°E. The signature of the structure extended along the south-to-north direction from lower latitudes, migrated to earlier local times with increasing latitude, and strengthened above 30°N. Tidal analysis using historical FPI data revealed that these structures were often seen during previous December solstices, and that they are much stronger for lower solar flux conditions, consistent with an upward-propagating tidal origin.

1. Introduction

Neutral wind dynamics play an important role in determining the state of the ionosphere-thermosphere (I-T) system due to the strong effect that they exert on global plasma distribution along magnetic field lines. Middle and upper thermospheric winds are primarily driven by the daily absorption of solar ultraviolet and extreme ultraviolet radiation which ultimately create horizontal global pressure gradients with subharmonics of a solar day that are generally called atmospheric tides (Forbes, 1982, 1995; Kato, 1980; Richmond, 1983). Dominant tides are the diurnal (24-hr) and semidiurnal (12-hr) migrating components. They are sun-synchronous from the vantage point of a fixed observer on the ground and exhibit a westward phase velocity, that is, they migrate with the apparent motion of the sun. Conversely, non-migrating atmospheric tides do not follow the apparent motion of the sun. They can propagate eastward or westward and can have the same periods as the migrating tides. Thus, whereas the effects of migrating tides are observed in day-night variations, non-migrating tides are responsible for longitudinal variations.

A general nomenclature employed to denote these tides is given by their period and wavenumber. Under this framework, for instance, diurnal migrating tides and eastward propagating diurnal non-migrating tides with wavenumber 3 are written as DW1 and DE3 respectively. The resultant tidal dynamics have been extensively

studied with observations and simulations (e.g., Forbes et al., 2008; Truskowski et al., 2014 and references therein).

Solar radiation absorption by water vapor and latent heating associated with convection in the troposphere are important sources of non-migrating tides (Zhang et al., 2010a, 2010b), both of which are strongly influenced by land-sea differences. Another important mechanism for the generation of non-migrating tides is the non-linear interaction between atmospheric tides and waves or between waves (Forbes, 2021, and references therein). In this mechanism the interaction between two waves yields two secondary waves with frequencies and zonal wavenumbers that are the sum and difference of those of the primary waves. For example, Hagan et al. (2009) found that non-linear interactions between DE3 and DW1 produced SE2 and a stationary planetary wave with wavenumber 4 (SPW4). Along similar lines, Jones, Jr. et al. (2013) showed that longitudinal variations in the ionospheric plasma in the form of SPW1 combined with the DW1 component of the thermospheric wind circulation could generate non-migrating tidal components D0 and DW2 from hydromagnetic plasma-neutral coupling. They also showed that these effects were stronger for higher solar flux conditions, consistent with similar findings using Challenging Minisatellite Payload (CHAMP) observations (Häusler & Lühr, 2009) and the modeling work of Häusler et al. (2010).

Different satellite missions have provided observations crucial to our current understanding and prediction of neutral wind dynamics. One of the more important efforts was undertaken by the Horizonal Wind Model (HWM14; Drob et al., 2015) which assimilated an extensive database of satellite- and ground-based observations to represent the thermospheric general circulation. As Drob et al. (2015) indicate, HWM14 accounts for recurring global-scale stationary planetary waves and the diurnal, semidiurnal and terdiurnal migrating tides. Chu (2019) compared neutral wind predictions from this empirical model and ground-based observations from different Fabry-Perot interferometers (FPIs) located at Pisgah Astronomical Research Institute (35.20°N, −82.85°E), Urbana Airglow Observatory (40.17°N, −88.16°E), Oukaïmeden Observatory (31.20°N, −7.9°E) and South African Astronomical Observatory (32.28°S, 20.81°E), and found general agreement with predictions if they were closer to the site location where HWM was constrained by prior observations used in the model construction. Chu (2019) showed that discrepancies with observations could be reconciled by optimizing the phase of the terdiurnal tidal components within the model using Taylor diagrams and an optimization scheme based on neutral wind observations, a result elaborated on by Ojo et al. (2022).

More recently, observations made by the suite of instruments on board NASA's Ionospheric Connection Explorer (ICON; Immel et al., 2018) satellite provide measurements of neutral winds, ion drifts, and plasma density and have been used to study atmosphere-ionosphere coupling during 01–21 January 2020 (Forbes et al., 2021). They showed that the variability of the low-latitude DE3 zonal winds at 106 km, and wave-4 equatorial vertical drifts and zonal and meridional winds at 295 km, were due to non-linear interactions between the 2- and 6-days planetary waves and ∼3-days ultra-fast kelvin waves. Moreover, they found evidence of additional non-linear interactions between non-migrating tide DE3 and migrating tide DW1 that explain the increasing magnitudes of SE2 above 120 km during this period. They suggest that SE2 can subsequently interact with DW1 variations in winds and ion drag to non-linearly generate DE3 and the eastward propagating terdiurnal tide TE1. The additional DE3 can also generate SPW4 in situ as well as a longitudinally symmetric quatradiurnal tide that is, Q0. Maute et al. (2023) analyzed ICON neutral wind observations from the August-September 2020 period following a Hough Model Extension tidal analysis. They showed that SW2 was upwardly propagating from 110 to 250 km in the upper atmosphere, and that the latitudinal and temporal variations of DW1, TW3 and QW4 migrating tides were closely related to that of SW2. They suggested that TW3 and QW4 were non-linearly generated by the interaction between DW1 and SW2, and SW2 and TW3 respectively.

The wave-wave interactions noted above suggest a degree of complexity within the dynamics of the coupled I-T system that was previously unappreciated and that remains unexplored.

By analogy with the TE1, TW4, and TW5 terdiurnal tides that originate from interactions between migrating and non-migrating diurnal and semidiurnal tides in the lower thermosphere (Lühr & Manoj, 2013; Moudden & Forbes, 2013), it seems reasonable to assume that such interactions also occur within the middle and upper thermosphere. Indeed, the additional presence of diurnal harmonics in the nonlinear ion drag term in the momentum equations (e.g., Jones, Jr. et al., 2013) combined with longitudinal dependence of the magnetic field, suggest that a whole host of high-order tidal harmonics likely exist in the I-T system. Outstanding questions include whether such high-order harmonics are observable, and if they measurably contribute to I-T complexity. The present paper

combines space-based and ground-based observations at low to middle latitudes to answer these questions in the affirmative for the first time.

In the next section, we describe the instrumentation utilized, and in Section 3 we present the nighttime wind structure observed by ground-based FPIs that motivated the present study. In Section 4 a tidal analysis methodology is described, and in Section 5 this is applied to ICON/MIGHTI wind observations to place the ground-based observations into a global context. This global context includes a decomposition into non-migrating tides that confirms the origin of the structures observed form the ground. Section 6 summarizes our conclusions.

2. Instrumentation

The midlatitude thermospheric neutral wind observations used in this study were made using ground-based FPIs located at Boulder, CO (40°N, 105°16′W, dip latitude ∼49°N), Urbana Airglow Observatory in Urbana, IL (40°17′N, 88°16′W, dip latitude ∼51°N), Millstone Hill Optical Laboratory in Westford, MA (42°36′N, 71°30′W, dip latitude ∼50°N) and Oukaïmeden Observatory in Morocco (31°12′N, 7°52′W, dip latitude ∼24°N) and from the spaceborne measurements made by the Michelson Interferometer for Global High-resolution Thermospheric Imaging (MIGHTI; Englert et al., 2017, 2023) onboard the National Aeronautics and Space Administration's (NASA's) Ionospheric Connection Explorer (ICON, Immel et al., 2018) satellite.

Both instrument types estimate the bulk velocity of the thermalized atomic oxygen in the thermosphere by measuring the Doppler-shifted spectra of the 630-nm airglow emission line. Each instrument integrates the received airglow emission along specific line-of-sight (LOS) directions. From the ground, the FPIs resolve the neutral wind velocity along the cardinal directions as well as toward zenith, corresponding to geographic locations of ∼2.5° latitude and longitude around the FPI site location and over the FPI site location, respectively. These directions are cycled throughout the night. At Urbana and Morocco, the integration times are dynamically calculated based on the airglow intensity and generally range from 30 s to 4 min. The integration times at Millstone Hill and Boulder are fixed to be 3 and 5 min, respectively. A 632.8-nm HeNe laser observation is included during each cycle with typical integration times of 30 s to monitor instrumental drift. The etalon clear aperture, spacer gap and number of interferometric orders are 10 cm, 1.5 cm and 10 for the Urbana FPI, 7.5 cm, 1.5 cm and 10 for the Morocco FPI, 12.8 cm, 1.0525 cm and 5 for the Millstone Hill FPI and 10 cm, 2 cm and 14 for the Boulder FPI. The optical design and analysis of the images for the Urbana and Morocco FPIs were described in Makela et al. (2012, 2013) and Harding et al. (2014), and for the Boulder FPI in Wu et al. (2004). Figure 1 shows the geographic locations of the cardinal points of measurement around the FPI sites, except for the Morocco site.

ICON/MIGHTI uses two separate Michelson interferometers to observe the oxygen airglow emission along orthogonal LOS directions pointing ∼45° and ∼135° from ram in the counter-clockwise yaw direction. ICON follows a 27° inclination orbit, allowing the remote observations to map to equatorial and mid latitude regions over all longitudes and solar local time (SLT) sectors for 15 times a day (Cullens et al., 2020; Forbes et al., 2021). Oxygen emissions from both the mesosphere and thermosphere are observed to provide altitude-resolved wind measurements from approximately 90 to 300 km altitude. Observations are made along the entire orbit and are representative of tangent points at each corresponding altitude. In this study, we consider measurements of the 630-nm emission made at thermospheric altitudes above 200 km. More details about the observing geometry and analysis can be found in Harding et al. (2017). Figure 1 shows the geographic locations of the orbit described by the tangential points observed by ICON/MIGHTI.

3. Data Presentation

We used version 5.0 of the ICON/MIGHTI level 2.2 data products. These data products correspond to estimates of the zonal and meridional winds inferred from combining the LOS measurements made by the two orthogonally observing ICON/MIGHTI instruments. They were derived following the methodology described by Harding et al. (2017) and Englert et al. (2023). The quality flags considered in the present study are those higher than 0. As an additional quality-control, measurements derived from LOS observations that crossed the terminators were not included. In order to compare the height-integrated measurements provided by the ground-based FPIs with the height-resolved ICON/MIGHTI wind vectors, we used the procedure described by Makela et al. (2021). According to this procedure, the volume emission rate is normalized and used as weights in the calculation of the height-integrated ICON/MIGHTI wind vectors.

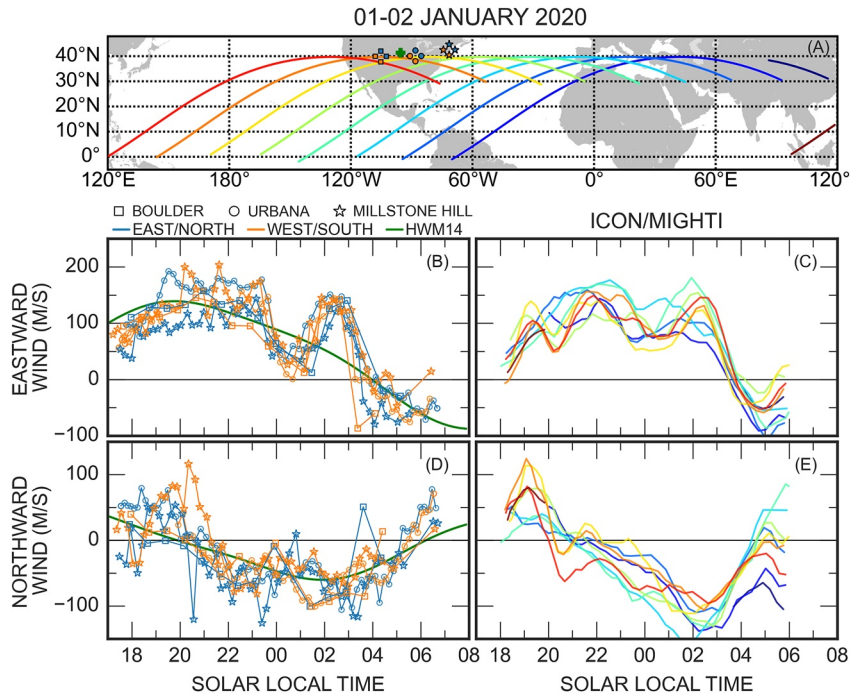

Figure 1. Thermospheric winds during the night-time period of the 01–02 January 2020 for the 120°E−240°E longitudinal sector. (a) Orbit tracks of tangential points of the ICON/MIGHTI red filter observations shown by rainbow-colored lines, and the geographic locations of cardinal pointing directions over the Fabry-Perot interferometer (FPI) sites located at Boulder (square), Urbana (circle) and Millstone Hill (star). East/North and West/South locations shown as blue- and orange-colored symbols respectively. Reference location for HWM14 predictions is shown as green cross. (b) Eastward winds over the east and west of the FPI sites shown in blue and orange respectively. Each FPI site location follows marker definition in (a). (c) ICON/MIGHTI eastward wind observations along the orbit tracks shown in (a). (d) Northward winds over the north and south of the FPI sites shown in blue and orange respectively. Each FPI site location follows marker definition in (a). (e) ICON/MIGHTI northward wind observations along the orbit track shown in (a).

For the ground-based FPI observations, individual measurements having statistical uncertainties larger than 25 m/s and temperature values lower than 500 K were removed (Fisher et al., 2015; Makela et al., 2012). Millstone Hill FPI observations with quality flags of 0 and 1 were used. In addition, the Urbana, Boulder and Morocco FPI observations made during cloudy conditions, as determined by collocated cloud sensors, were removed. Furthermore, at Urbana and Morocco, low intensity measurements were removed from the analysis. Only observations made during geomagnetically quiet conditions of Kp <3 during the time of the observations and 6 hr before were considered. More details on the comparison of the viewing geometries of these two different observing platforms and of the zero-wind phase reference for ICON/MIGHTI can be found in Makela et al. (2021). FPI winds from September to April were collected and a database was created consisting of a total of 27,100 hr of observations. Observations from November 2009 to November 2020 were included from the Boulder FPI; from September 2012 to March 2021 for the Urbana FPI; and from December 2009 to November 2020 for the Millstone Hill FPI. These observations are fairly distributed throughout these months with the lowest number of observations in April for the Millstone Hill FPI. We also used 36 nights of observations from December 2019 to January 2020 for the Morocco FPI.

Figure 1 shows the eastward and northward winds from the FPI sites in the left column of the bottom panels and the corresponding height-integrated ICON/MIGHTI winds in the right column during the night of 01–02 January 2020 when a strong ±100 m/s oscillation in the eastward winds occurred between 23:00 and 04:00 SLT. For further study of this structure and to further understand its origin and characteristics, we limited our ICON/MIGHTI and historical FPI observations to the December solstice except in Section 5.2.2 where equinox FPI observations were included for a contrast with December solstice results.

Figure 2 shows our database of thermospheric winds of ground-based FPI and ICON/MIGHTI observations during the December 2019–January 2020 solstice period. For MIGHTI, all data from 20°N deg to the northern

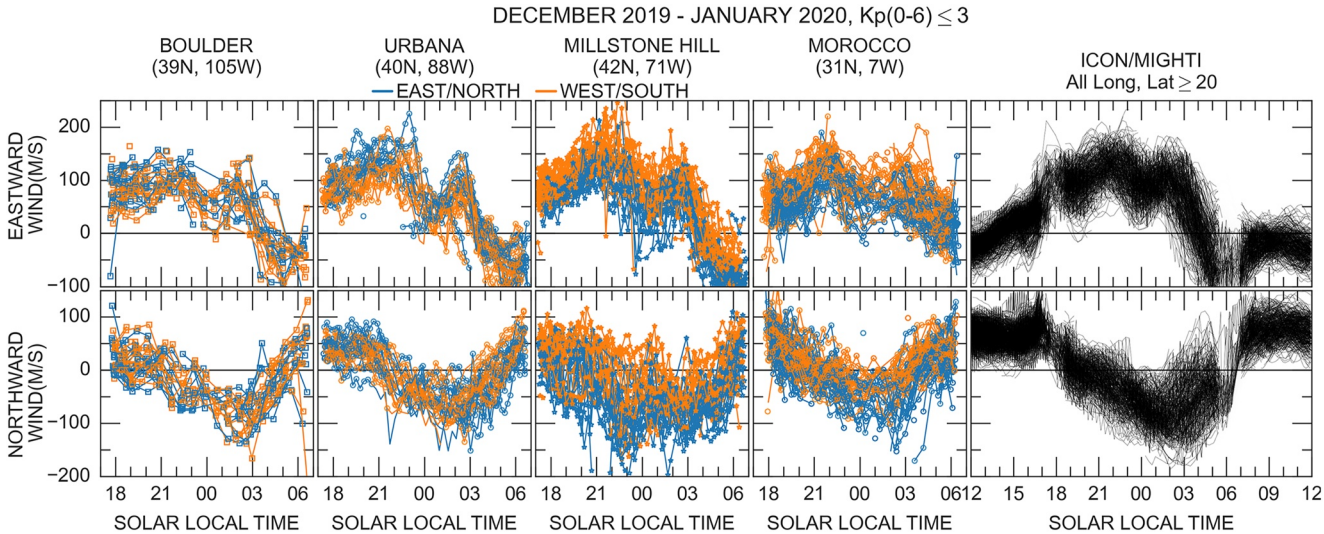

Figure 2. Eastward and northward thermospheric winds during the December 2019–January 2020 as observed by the Boulder, Urbana, Millstone Hill, and Morocco FPIs and ICON/MIGHTI observations. ICON/MIGHTI observations at the solar terminators are shown as transparent.

extent of the observations at ∼42° latitude are shown. A persistent structure is evident during this period at night. The SLT variation of the eastward winds displays a similar structure in the FPIs and the ICON/MIGHTI observations. This structure is also present over Morocco, located 10° lower in latitude than the other FPI sites in North-America. ICON/MIGHTI observations follow the same pattern. Northward winds show SLT variations similar to the FPIs. The long-lasting persistence of this structure over many nights leads us to consider possible tidal origins for the structure.

4. Methodology and Analysis

A tidal decomposition was applied to the ICON/MIGHTI wind data to assess the tidal nature of the structure evident in Figures 1 and 2. Within this framework, the horizontal wind field, $\tilde{w}$, can be mathematically expressed as a sum of individual tidal components,

$$\tilde{w} = \sum_{n} \sum_{s} A_{n,s} \cos\left[n\Omega t + s\lambda - \phi_{n,s}\right]$$

where n, s denote the subharmonics of a solar day and zonal wavenumber, respectively. A, ϕ are the amplitude and phase of the corresponding tidal component at a given latitude and height. t and λ are universal time and longitude respectively. $\tilde{w}$ is the estimated component of the wind. For example, $[n, s] = [3, -2]$ corresponds to TE2 for a terdiurnal eastward propagating tide with wavenumber 2. If n and s are equal, the tidal oscillation moves synchronously with the sun and is referred to as a migrating tide. Oscillations with $n \neq s$ are known as non-migrating tides since they are solar asynchronous. A more detailed description of this methodology can be found in Forbes (1995).

In this study, we focus on the non-migrating components with $n \geq 3$ since, as shown below, the structure looks to be fixed in SLT and appears to contain smaller than 12-hr periodicities. For these tides, we followed the methodology used by Moudden and Forbes (2013) who performed tidal fitting of consecutive days of observations within windows covering 8-hr of continuous SLT at all longitudes. For ICON, 18-days of continuous observations are required to cover 8-hr of SLT according to the rate of precession of the ICON satellite for each ascending and descending node (see Figure 2 of Forbes et al. (2021)). Similarly, 41–48 days of data are required to extract diurnal and semidiurnal tides from ICON data, depending on the range of latitudes covered. We used shorter fit spans for the $n \geq 3$ tidal components since it was found that they exhibited a degree of day-to-day variability that would have resulted in phase cancellation and amplitude suppression if their determinations were based on the longer fits spans required for extracting the diurnal and semidiurnal tides.

Specifically, we binned our height-integrated ICON/MIGHTI database for each wind component into 15 UT min and 15° longitude bins. The wavenumber range of interest goes from −6 to 6. We follow the following procedure:

1. We use 48-days windows to estimate all tidal components from diurnal ($n = 1$) up to quatradiurnal ($n = 4$) and identified components with magnitudes stronger than 2 m/s.
2. We fit diurnal and semidiurnal tidal components to the 48-days windowed data using the strongest tides previously selected.
3. We fit terdiurnal and quatradiurnal tidal components to the 18-days window residual data. These residuals were calculated by removing the previously fitted diurnal and semidiurnal baselines from sliding 18-days windowed data. We used the strongest tides previously identified in the fitting.

As previously stated, this procedure follows Moudden and Forbes (2013) who similarly calculated shorter than semidiurnal tidal components to residuals from a baseline within sliding windows. We also tested the procedure just outlined for different tidal combinations and found that no additional information was obtained when fitting higher-order tides for the purposes of the structure under study. We followed this procedure for the ascending and descending nodes for 6° latitude bins spaced every 3° and ordered the results in SLT. Note that different node and latitudinal data sets locate the moving 8-hr windows into different SLT periods. The tidal reconstructions shown in subsequent sections were separately reproduced for each node set and averaged to represent an overall reconstruction.

It is important to mention that the tidal spectrum for each sliding window and for each node set can provide different tidal magnitudes for different wavenumbers depending on the structure present in the resultant 2D space. This variability is due to the variability present on each node set and to the nature of the sliding window which can partially display different regions of the structures present in the data as it slides in time. The lack of observations around the solar terminators is also challenging for our methodology. These factors contribute to an imperfect match between tidal reconstructions and the actual data. Nevertheless, and despite its limitations, our tidal reconstructions capture the most salient features and serve as a powerful tool to understand the sources and origins of the main structure under study.

The ground-based wind observations followed a similar analysis to obtain terdiurnal and higher order diurnal components. Given that the FPIs point to specific locations in the sky, they integrate along specific emitting volumes in the upper atmosphere and do not provide tidal wavenumber information. Their local night-time coverage of 10–12 hr during December solstice also prevents the estimation of longer local time harmonics. Other studies have used orthogonal spline functions to fit climatological averages with less than 12 hr of coverage providing good reconstruction of their SLT dependence (e.g., Alken, 2009; Brum et al., 2012; Emmert et al., 2003). We used a 60-days running window every 7 days for each cardinal direction data set. The representation of longer-period tidal components was obtained by smoothing 4-months climatological averages. The residuals from subtracting these baselines out of the 60-days averages was fitted to terdiurnal and quatradiurnal components.

5. Results and Discussion

5.1. Persistent Structure in Thermospheric Winds

The midlatitude thermosphere presented a large and fixed-in-SLT structure during the December 2019–January 2020 period. Figure 1 shows this structure seen from both observing platforms. The FPI winds show eastward flow of ∼100 m/s around 18:00 SLT. They gradually increase to peak magnitudes of ∼170 m/s from 20:00 to 22:00 SLT before decreasing to a minimum of ∼10 m/s around 00:30 SLT. They later increase back up to ∼150 m/s at 02:00 SLT before finally decreasing and reversing to 50 m/s westward around 04:00 SLT. The same structure is observed by ICON/MIGHTI with similar SLT dependence, having a peak eastward wind of ∼150 m/s between 22:00 and 02:00 SLT and decreasing to ∼50 m/s around midnight. Winds measured by ICON/MIGHTI also decrease and reverse to about the same magnitude of ∼50 m/s westward before sunrise.

Likewise, the meridional winds during this period are consistent between the different measurement platforms. They are northward with magnitudes of ∼50 m/s in the early night, gradually decreasing in magnitude before reversing around 20:30 SLT except for the point south of Millstone Hill, which reversed 1 hr later, reaching peak magnitudes of about 80 m/s southward between 22:00 and 01:00 SLT and then quickly decreasing in magnitude before reversing to northward around 05:30 SLT. The meridional wind observations made by the FPIs show small

oscillation-like structure throughout the night. The magnitudes of these oscillations are small, ∼30 m/s, except for the one point south of Urbana. These oscillations are not, however, apparent in the spaceborne observations.

Figure 2 shows the persistence of this structure during this December solstice period as observed by different FPIs and ICON/MIGHTI. Throughout this period, zonal winds are eastward and reach maximum magnitudes around 21:00 SLT, decrease in magnitude and then increase again to reach a second maximum around 02:00–03:00 SLT before reversing to westward winds prior to local sunset. The variability is larger over Millstone Hill than over the other FPI sites. Similarly, the meridional winds reverse southward early in the night, increase to 20:00–23:00 SLT, reduce their magnitude around midnight, and then strengthen southward after 01:00 SLT. They reach peak magnitudes of ∼120 m/s around 02:00–03:00 SLT except over Millstone Hill where strong variability of these winds is observed throughout the night and over Morocco where the structure in the winds reach peak magnitudes around midnight. The zonal wind observations shown in Figure 2 show that the structure has strong longitudinal variations of peak values. They also showed characteristic features for three different SLT sectors: early night (20:00–23:00 SLT), midnight (23:00–01:00 SLT), and post-midnight (01:00–03:00 SLT), corresponding to the main features observed in the structure.

The FPI wind errors for the data presented in Figures 1 and 2 are steady in magnitude throughout the night for both wind components except for the Boulder and Morocco FPIs. They ranged from 8 to 10 m/s for Boulder and from 13 to 20 m/s for Morocco. The Urbana FPI shows errors of 8 m/s and the Millstone Hill FPI shows errors of 3 m/s. Note that these optical systems use different optical design parameters like etalon clear aperture among others (see Section 2), and that they undertake different parameter estimation techniques. Nevertheless, these statistical errors are less than 20% error with respect to wind magnitudes, in particular with respect the eastward winds where the structure under study is evident. Similarly, ICON/MIGHTI wind errors are of 7 m/s (3 m/s) during the night (day) with stronger uncertainties around midnight hours of ∼10 m/s for both wind components. More on the sources of these errors is provided in Englert et al. (2023).

5.2. Tidal Decomposition

5.2.1. Analysis Using ICON/MIGHTI Observations

In order to enable a more detailed analysis of the tidal contributions to the structure described above, each wind component of the ICON/MIGHTI observations was fit to estimate the terdiurnal and quatradiurnal tidal components following the procedure described in Section 4. This procedure was used for the 2019–2020 December solstice period. Figure 3 (Figure 4) illustrates this procedure using the ascending (descending) nodes of the eastward (northward) winds for the latitudinal bin of 36°–42° and centered on the 02 January 2020. The first step of our procedure selects strongest tidal components; however, tidal magnitudes will be reported from steps 2 and 3.

Figure 3 shows results of our tidal decomposition procedure for the ascending node set of zonal winds for the nights of 14 January 2020 and 02 January 2020. For these two nights, the 8-hr sliding time windows are centered around 21:00 and 02:00 SLT respectively. The time sectors of these days can be used to study the tidal components around the early night and post-midnight sectors where the characteristic features of the structure under study are observed as discussed in Section 5.1. The top and bottom row show the binned and fitted eastward winds respectively. The time periods around the solar terminators are grayed-out and shown in the top and bottom panels for display purposes only and are not used in further analysis due to the challenges presented in reliably interpreting the ICON/MIGHTI data during these times. These time sectors were not considered as outlined in Section 3. The panel on the left shows results for the diurnal and semidiurnal fits following step 2. The second and third columns show the binned residuals and corresponding terdiurnal and quatradiurnal fitted values following step 3.

The non-migrating tidal spectra obtained for the diurnal and semidiurnal fits showed magnitudes of 11, 3.2, 3.1, 2.8, and 2.7 m/s for D0, DE2, DE1, DW2, and DE5 respectively, and of 8, 4.5, 4, 3.5, and 2.4 m/s for SE2, SE3, SW4, S0, and SW1 respectively. The migrating tide magnitudes are 81.5 and 7.5 m/s for the diurnal and semidiurnal tides respectively. The corresponding tidal reconstruction is shown in the bottom panel of the first column. Our results show that a 4-peaked structure occurs in the pre-midnight sector and at early morning local time sectors in the SLT frame which can be explained by the strong SE2 and SW4 tidal components. Similarly, the residuals observed in the second column are very small and so the resultant fit is also almost zero. However, this time window captures some of the midnight morphology and so the contribution of the higher order components

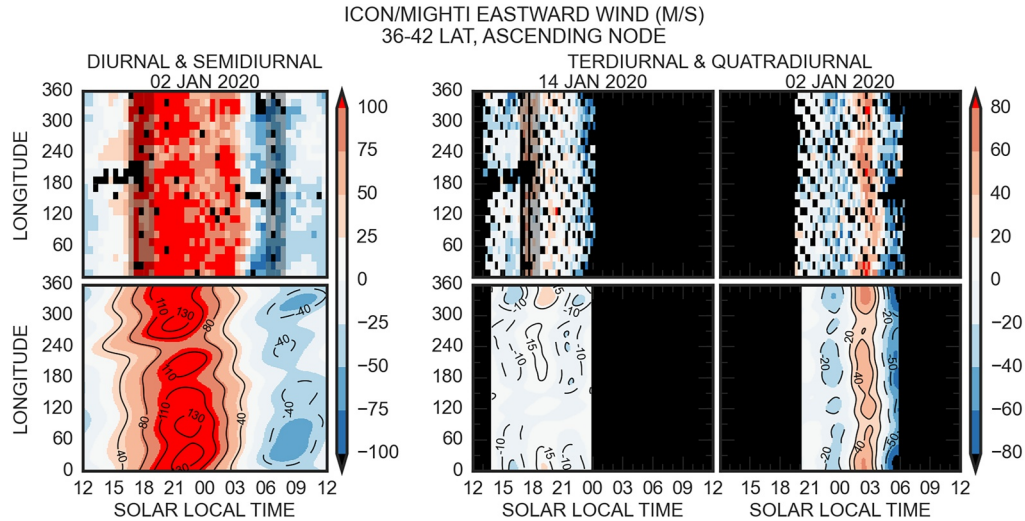

Figure 3. (Top) Binned ICON/MIGHTI observations (left) and residuals from diurnal and semidiurnal baselines (right). (Bottom) Reconstructions based on fitted zonal winds. The bottom left most column shows the tidal reconstruction for diurnal and semidiurnal components for the 48-days analysis centered on 02 January 2020. The panels on the bottom right show the tidal reconstructions based on the residuals from the diurnal and semidiurnal fit for both the 14 January 2020 and 02 January 2020 periods. The solar terminator data are shadow in the binned and residuals averages but not used in the analysis. As stated in the text, this procedure fits diurnal and semidiurnal tidal components at the first step, and subsequently fits terdiurnal and quatradiurnal components to residuals from the first fit.

is not zero. On the other hand, analogous results for the day of 02 January 2020 showed a strong contribution of terdiurnal and quatradiurnal components. As observed in the bottom panel of the third column, the longitudinal variation of the structure around the post-midnight sector is a double-peak in longitude around 120°–240°E and 300°–30°E longitudinal sectors. The non-migrating terdiurnal tides obtained by this analysis are 6, 4, 4, 3.2, and 2.8 m/s for TW5, TW6, TW2, TE2, and TE4 respectively, and for the quatradiurnal tides are 8, 7.7, and 3.5 m/s for QW3, QW6, and QW2 respectively. The migrating tide magnitudes were of 31 and 34 m/s for the terdiurnal and quatradiurnal components respectively.

Figure 4 shows corresponding results for meridional winds centered on the nights of 31 December 2019 and 06 January 2020. These days provided SLT windows centered at 05:00 and 00:00 SLT, respectively as shown in the right panels. The diurnal and semidiurnal non-migrating spectra for the diurnal and semidiurnal tides showed

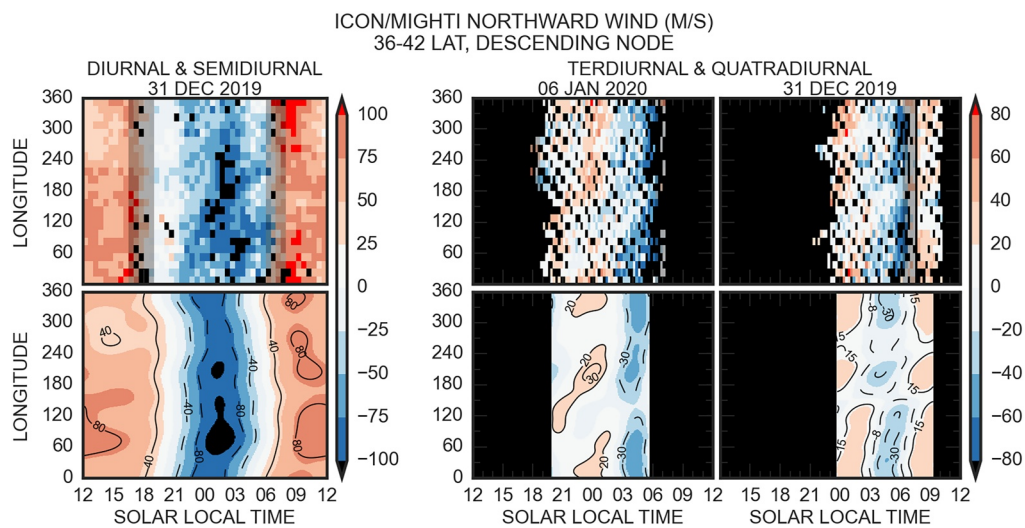

Figure 4. Same as Figure 3 but for meridional winds.

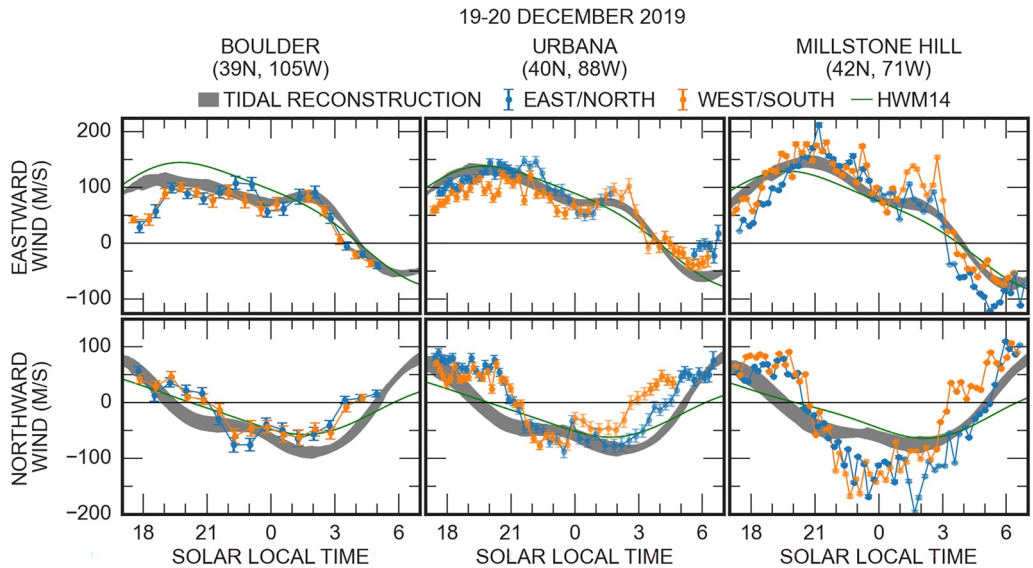

Figure 5. Longitudinal comparison of zonal and meridional thermospheric winds from ground-based observations, spaceborne tidal reconstructions (shadowed) and HWM14 predictions (green) for the Boulder (left), Urbana (mid) and Millstone Hill (right) Fabry-Perot interferometers in the North American sector during the night of 19–20 December 2019.

magnitudes of 11.6, 5, 4.4, 3, 2.9, and 5.2, 4.3, 3.5 for D0, DW2, DE1, DW4, DE4, and SW3, SW4, S0 respectively. The migrating tidal magnitudes were 81.9 and 29 m/s for DW1 and SW2, respectively. The bottom panel shows departures from the top fitted baseline around 20:00, 00:00 SLT and from 03:00 to 06:00 SLT at night and also around 09:00 SLT and 15:00 SLT during daytime. Note that these values are obtained for a timespan of 48-days. We will focus our analysis on the midnight and post-midnight sectors that showed southward and northward departures from the diurnal & semidiurnal baselines. The right panels show the corresponding fitted and binned averaged for the time windows around the previously mentioned SLT sectors. The top and bottom panels show the longitudinal structures in the mid- and post-midnight sectors. The midnight sector shows a double structure of northward winds with strongest magnitudes around 60°–300°E and 180°–240°E longitudinal sectors. Note that this longitudinal variation is similar to the post-midnight longitudinal variations for the eastward winds as shown in the right column of Figure 3. Also, the data show a southward wind in the early night sector from 19:00 to 21:00 SLT with similar longitudinal variations. Similarly, the bottom panel in the last column of Figure 4 shows a strong southward wind that extends from 120°E to 300°E from 06:00 to 03:00 SLT. The non-migrating tides responsible for these structures are T0, TW2, TW5, TW1, TE1 and QW3, QW5 with magnitudes of 7, 6.4, 4.5, 4.1, 4 and 6, 2.3 m/s respectively. The migrating tide magnitudes were 28.8 m/s and 11 m/s for the terdiurnal and quatradiurnal components, respectively.

For cross-validation of our tidal analysis procedure, we compare tidal reconstructions derived using ICON/MIGHTI observations with the ground-based FPI data set. Figure 5 shows the comparison for the night of 19–20 December 2019. As before, the orange and blue circles show the FPI observations made in the cardinal directions, the solid green line shows HWM14 results for this night, and the shaded regions shows the ICON/MIGHTI tidal reconstructions using the tidal parameters obtained from our procedure centered on this night. Each column shows observations and reconstructions from west to east across the North American sector for the Boulder, Urbana, and Millstone Hill FPIs. While the structure, most evident in zonal winds between 21:00 and 04:00 SLT, is not seen in the HWM14 results it is seen in the tidal reconstructions.

As shown in Figure 5, the structure present throughout this period is reproducible by considering the terdiurnal and quatradiurnal tidal components derived from tidal analysis of ICON/MIGHTI observations. The pre-midnight eastward wind increases from west to east in both the ICON/MIGHTI reconstructed wind and in the ground-based observations. This is also consistent with results in Figure 3. On the other hand, the post-midnight eastward wind peak magnitudes, which are mainly driven by shorter tidal components as previously discussed, decrease from west to east that is, 73, 56, and 50 m/s around 02:30–03:00 SLT for the Boulder, Urbana, and Millstone Hill FPIs, respectively, for the tidal reconstructions whereas the ground-based observations show an

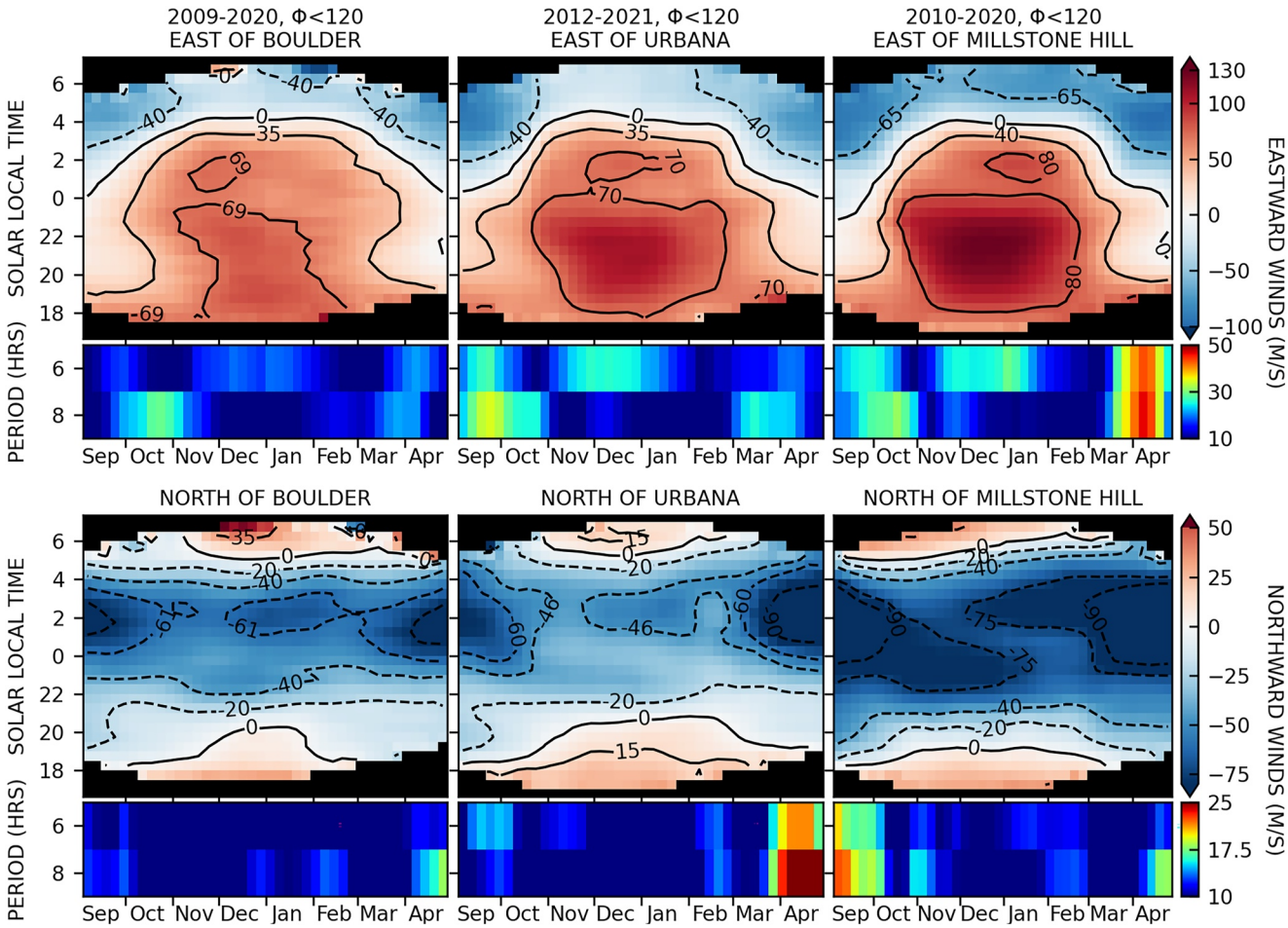

Figure 6. Climatological 60-days averages and corresponding tidal spectra of night-time thermospheric zonal and meridional winds over the east (top) and north (bottom) of the Boulder (left), Urbana (mid) and Millstone Hill (right) Fabry-Perot interferometer site.

increase of the post-midnight eastward wind peak magnitudes from west to east. The decreasing eastward wind in the eastern North American sector is also observed in Figure 7 and the opposite effect in the ground-based observations is also observed in Figure 2. This might be a consequence of the difference in the viewing geometry and the corresponding atmospheric scattering across the LOS observations of each observing platform.

Our tidal analysis shows the complex tidal spectrum responsible of the structure under study. Further analysis of our results, discussed below, suggest that a tidal origin of these structures due to nonlinear tidal interaction. We will suggest nonlinear interactions combined with longitude-dependent ion drag adds additional complexity to the in situ generated tidal spectrum.

5.2.2. Analysis Using FPI Observations

Our results indicate terdiurnal and quatradiurnal tidal origins for the structures observed during the 2019–2020 December solstice. We performed a tidal analysis over historical observations from the ground-based instrumentation to further assess this statement using several years of data. Figure 6 shows a climatological overview of the eastward and northward winds looking to the east and north of the Boulder, Urbana, and Millstone Hill FPIs for lower solar flux ($\phi < 120$) and geomagnetically quiet (Kp < 3) conditions over 6 hr preceding the time of the observations. The geomagnetic and solar flux conditions considered were chosen to match the conditions observed during the 2019–2020 December solstice. The top row shows climatological eastward wind averages from September to April, and the second row shows the tidal spectra derived from the averages in the top panels. The third and bottom panels show similar results for the northward winds. The climatological averages were obtained from a 60-days, running 7-days window. As mentioned before, we considered a smoothed version

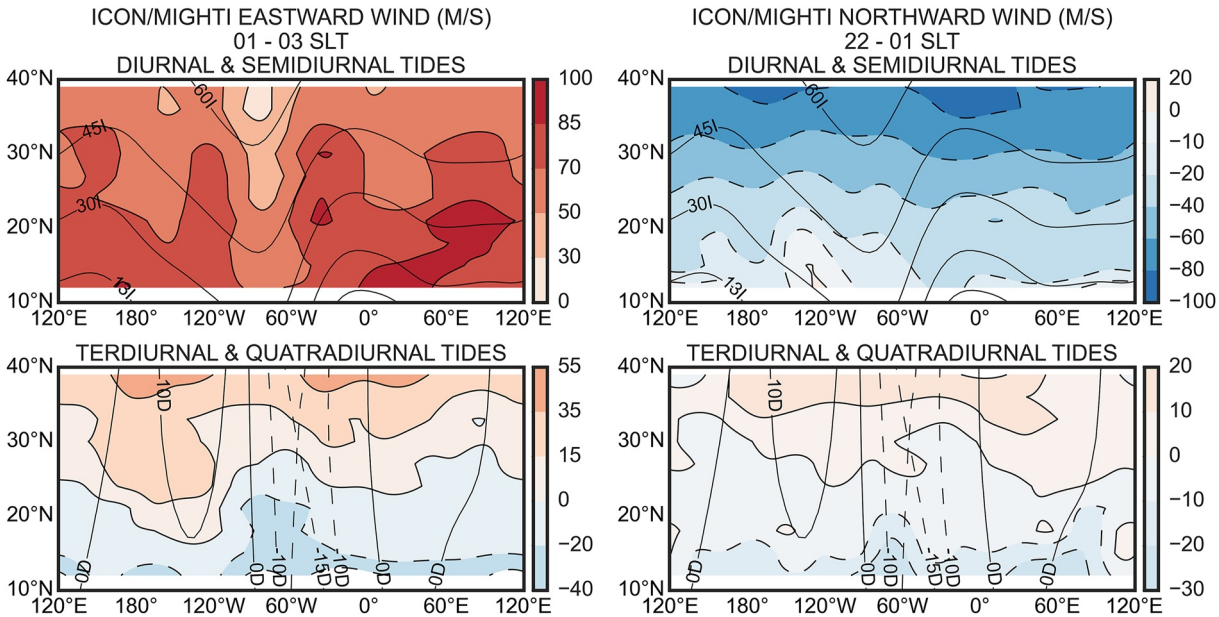

Figure 7. Longitudinal and latitudinal variations of the diurnal and semidiurnal tides (top row) and of the terdiurnal and quatradiurnal tides (bottom row) of the ICON/MIGHTI zonal and meridional winds around the solar local time sectors of 01–03 (left column) and 22–01 (right column) respectively and during the December 2019–January 2020 period. Solid and dashed contours show positive and negative values of Earth's magnetic inclination (declination) in top (bottom) panels.

of 4-months climatological averages for a representation of longer tidal components, removed them out of the 60-days averages and estimated the spectra from the resultant residuals. The eastward winds shown in this figure are generally stronger to the east of Millstone Hill FPI than to the east of the Urbana FPI, and stronger to the east of Boulder, CO than to the east of Urbana, IL. The eastward winds are stronger around late December and early January and the eastward-to-westward reversal time shifts from midnight around the equinoxes to ∼04:00 SLT during December solstice. The terdiurnal tidal magnitudes around the equinoxes are 30 m/s, except for the vernal equinox to the east of Millstone Hill when they are about 45 m/s. The 6-hr tidal components are stronger during December solstice for both sites with amplitudes of 25 m/s. Similarly, the spectra for the meridional component of the winds show stronger terdiurnal magnitudes around equinoxes as well, and somewhat stronger quatradiurnal components during equinox and December solstice. Note that even with a small geographic separation from these sites, their spectra are seen to be similar but not identical, and in some cases significantly different, such as for vernal equinox. As shown by Forbes et al. (2003), ground-based observing instrumentation located at the same latitude will observe different tidal oscillations due to longitudinal variations in the non-migrating and migrating tidal components. This interpretation is consistent with our results.

5.3. Longitudinal and Latitudinal Variations of Tidal Components

From our results in Section 5.2.1, a double-peak structure in SLT is observed in both the residual data and tidal analysis at the highest-latitude enabled by the ICON/MIGHTI observations in the post-midnight eastward winds and mid-night northward winds. In order to understand the latitudinal extent of these structures and to provide insight into possible drivers, we used ascending and descending nodes separately and combined our results to observe the contributions and longitudinal and latitudinal variations of the shorter- and longer-period tidal components.

Figure 7 shows the longitudinal and latitudinal variations of the diurnal and semidiurnal (top panels) and terdiurnal and quatradiurnal (bottom panels) tidal contributions to the zonal (left panels) and meridional (right panels) winds around the 01:00–03:00 (left panels) and 22:00–01:00 SLT (right panels) respectively. The morphologies shown in these panels are strongly structured by Earth's magnetic field topology. For the zonal winds, the diurnal and semidiurnal tides have stronger magnitudes for decreasing latitudes. The magnitudes are weakest around 80°W longitude for 10°N–40°N latitudes with weakest magnitudes of about 23 m/s poleward of 34°N latitude. The midlatitude longitudinal variations are structured following the magnetic inclination and their weakest

magnitudes around 80°W coincides with both the longitudinal sector where the inclination shows its strongest longitudinal variation and the longitudinal sector of the decreasing side of the magnetic declination from 0° to −15°. The diurnal and semidiurnal tidal contributions are stronger for latitudes below 30°N. At the same time, the contributions of the terdiurnal and quatradiurnal tides are stronger for latitudes above 30°N and their longitudinal variations tend to be structured following the longitudinal variations of the magnetic declination. The terdiurnal and quatradiurnal eastward winds are strongest around the longitudinal sectors of 200°–120°W and 30°W–60°E. In the former longitudinal sector, it extends with decreasing magnitudes from 40 to 22 m/s up to latitudes of 20°N, and it extends up to 30°N latitudes with similar magnitudes within the latter longitudinal sector. Similar dual-peak structure is shown for lower latitudes.

These results show that the longer-period tidal contributions to the post-midnight eastward wind are dominant for latitudes equatorward of 30°N and that shorter tidal contributions are stronger for higher latitudes. Similarly, the midnight northward winds shown in the right column show similar results except that the magnetic inclination is not as effective in structuring the longitudinal variations for these tidal contributions. However, the shorter tidal contributions, as shown by the terdiurnal and quatradiurnal tides, seem to follow the double peak structure that is also present in the zonal winds, which are also structured by the magnetic declination of Earth's magnetic field. The results from these two SLTs show the latitudinal extent of different drivers in the thermospheric winds. The diurnal and semidiurnal tides dominate up to about 20°–30°N latitudes during this December solstice period whereas the shorter-period tides are strongest for higher latitudes suggesting an effective contribution from high-latitude regions. However, as we will see next, there are migrating tide contributions at lower latitudes that need to be considered in the analysis of the underlying competing processes during this period.

5.3.1. Tidal Migration From Lower Latitudes

As observed in Figure 7, the post-midnight structure in the eastward winds exhibits a longitudinal double structure that is stronger at higher latitudes. Our spectral analysis shows that the dominant components are TW1, TW5 and QW2, QW6 sorted from weaker to stronger, and that they are mostly responsible for the longitudinal double-peak structure observed in the SLT frame. Forbes and Wu (2006) found TW2 and TW4 non-migrating tides in the lower MLT region using MLS-UARS temperature observations and attributed them to nonlinear interaction between TW3 and SPW1. The interaction between two primary waves with two frequencies and two wavenumbers generates secondary waves with the sum and difference frequencies and wavenumbers (Teitelbaum & Vial, 1991). Expressing a wave in terms of $[n,s]$, the above interaction goes as follows: SPW1 × TW3 = [0,1] × [3,3] → [3,4] + [3,2] = TW4 + TW2. However, these products are just the result of the product of two cosines, which needn't necessarily represent an atmospheric wave per se. For instance, one term in the product could represent the diurnal, semidiurnal or terdiurnal component of ion drag, or the SPW1, SPW2, or SPW3 longitudinal variation of the magnetic field (e.g., Jones, Jr. et al., 2013). Our results, shown in Figure 7, also indicate an important role of the longitudinal variation of the magnetic field in the strengthening of these shorter tidal harmonics. Similarly, results in Section 5.2.1 showed strong migrating tides DW1, SW2, TW3, QW4, and non-migrating tides of DE2, SE2, SE3, and SW4 for the zonal winds. This spectrum suggests that the non-migrating structure under study might have a terdiurnal tidal origin, and that the quatradiurnal tides are the result of non-linear interactions between terdiurnal tides and a longer tidal component with $s = 1$, probably related to the magnetic declination or to DW1. Thus, as explained before, to obtain QW6 or QW2, we would need TW5 or TW1 non-linearly interacting with DW1. Similarly, TW5 would be generated by SE2 and SE3, and these three tidal components are found to be strong during this period. Similar spectral results were presented by Moudden and Forbes (2013) for the TW5 and SW4 tidal components in the MLT region which is also consistent with our results. However, they were observed to be related to a seasonal migration along the north-south direction.

Our analysis and observations also show a latitudinal migration of tides that might shed light on the source of the competing processes during this period. In order to evaluate the potential migration of tidal components, Figure 8 shows the binned residual and fitted reconstruction from 27°N to 39°N latitude of the eastward and northward winds centered on 27 December 2019. The bottom panels for the lowest latitude showed a strong eastward wind in the pre-midnight sector along with a strong dual-peak structure in southward winds around the 00:00–01:00 SLT sector. The eastward structure in the pre-midnight sector seems to weaken and a structure in the post-midnight sector starts building up in the 30°N latitudinal bin while the southward structure shows somewhat weakened magnitudes. In the 33°N latitudinal bin, the post-midnight double-peak structure in the eastward wind strengthens and moves slightly to earlier local times. Similarly, the southward wind structure slightly migrates to

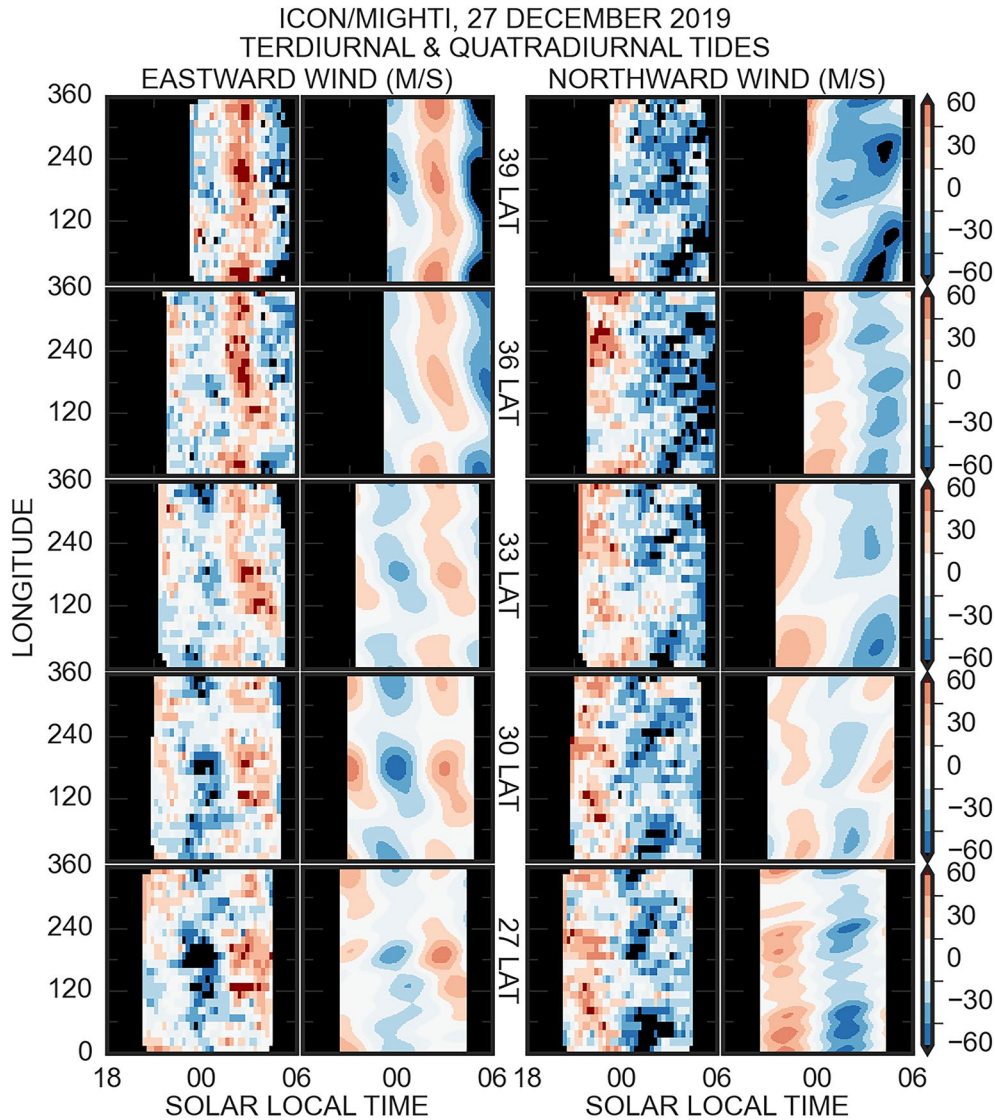

Figure 8. Latitudinal evolution of the longitudinal and solar local time dependent residuals and tidal reconstructions of ascending node of eastward (left) and northward (right) wind around 27 December 2019. The residual winds were removed from the 48-days diurnal and semidiurnal tides, and the tidal reconstructions were obtained by superimposing only the terdiurnal and quatradiurnal tidal components.

later local times. The structures in both wind components become strong and dominant at around 02:00–03:00 and 03:00–05:00 SLT for the zonal and meridional wind, respectively. The migration of these wind structures from lower latitudes show that these shorter-period tidal components migrate from lower latitudes and strengthen above 30°N, probably due to a stronger contribution from high latitude regions.

Previous work also relates to migration of tidal components from lower latitudes as in Moudden and Forbes (2013) for MLT region altitudes. They showed a seasonal migration of strong terdiurnal tides. This migration was attributed to a seasonal migration of SW4 and nonlinear interactions were suggested as the generation mechanism of the terdiurnal tides along its path. It started strong in the midlatitude southern hemisphere around the equinoxes, migrates northward crossing equatorial latitudes and reaches strongest magnitudes in the northern hemisphere around 01 January that is, middle of the December solstice in the northern hemisphere. Our results seem to have captured this migration during the December solstice. As we will later see, these structures are also related to lower solar flux conditions which might indicate an effective altitudinal penetration from the MLT region to thermosphere altitudes and as previously discussed, nonlinear interactions would play an important role

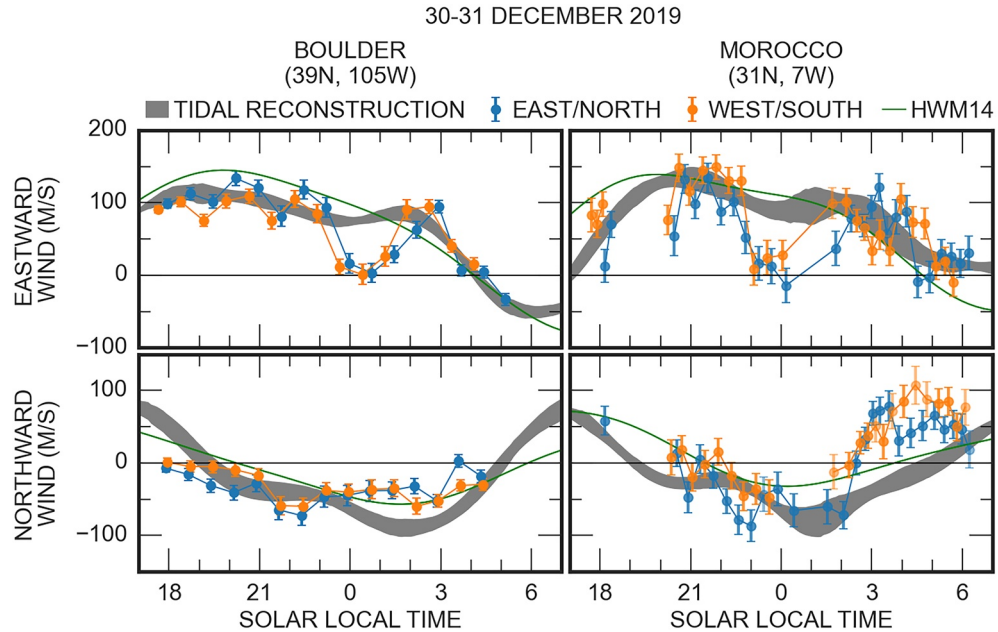

Figure 9. Latitudinal comparison of zonal and meridional thermospheric winds from ground-based observations, spaceborne tidal reconstructions (shadowed) and HWM14 predictions (green) over Boulder (left) and Morocco (right) Fabry-Perot interferometers during the night of 30–31 December 2019.

in the generation of shorter-period tidal components. The effects of the terdiurnal tides in the thermospheric temperatures and winds has also been reported in other studies. Crary and Forbes (1986) found that terdiurnal tidal components in the meridional winds enhanced the effect of the upwardly propagating semidiurnal tides to produce the midnight collapse of the ionosphere over Arecibo, Puerto Rico, an effect coming from below and closely related to enhancements of the airglow oxygen line (e.g., Nelson & Cogger, 1971) and to the Maximum Temperature at Midnight (e.g., Faivre et al., 2006; Herrero & Meriwether, 1980; Hickey et al., 2014; Martinis et al., 2013; Meriwether et al., 2008; Mesquita et al., 2018). Dandenault and Richards (2015) also reached similar conclusions. These studies suggested latitudinal migration of the effects of the terdiurnal tidal components over the thermosphere consistent with findings in Moudden and Forbes (2013). Our results are consistent with their findings in the northern hemisphere around late December–early January period. However, prior ground-based observations of the neutral wind had not recognized such a persistent feature, nor is it seen in the climatological winds as represented by HWM14. Also, the SLT tidal migration and its latitudinal dependence shown in Figure 8 show that these effects might be onset by tides along the meridional direction driven by effects coming from lower latitudes.

To further assess this migration from the ground-based perspective, we compared our tidal reconstructions of the night-time thermospheric wind at two different latitudes using observations from the Boulder FPI in North America and Morocco in northern Africa. Figure 9 shows the eastward and northward wind for the Boulder FPI located at (39°N, 105°W) and Morocco located at (31°N, 7°W) for the night of 30–31 December 2019. The ground-based observations show eastward winds throughout the night and reversal times to westward winds around 04:00 and 07:00 SLT for Boulder and Morocco respectively. The double-peak structure in Morocco is also observed with eastward magnitudes around 150 m/s from 20:00 to 23:00 SLT, weakest eastward winds around midnight, and again eastward winds of 100 m/s around 02:00–04:00 SLT. Similarly, the meridional winds are westward throughout the night for Boulder and Morocco FPIs with reversal times to northward directions in earlier local times for Morocco at 02:30 SLT than for Boulder which are close to 04:00 SLT. The post-midnight meridional wind is southward around 01:00 SLT over Morocco and reverse to northward from 03:00 to 06:00 SLT. Similarly, post-midnight southward winds over Boulder seem to weaken around 03:00 SLT.

Our ICON/MIGHTI tidal reconstruction reproduces overall features of the structure in the eastward winds observed by ground-based FPIs, except around midnight where the reconstructions showed much weaker magnitudes of the variation seen in the ground-based data. Similarly, our tidal reconstructions for the northward wind

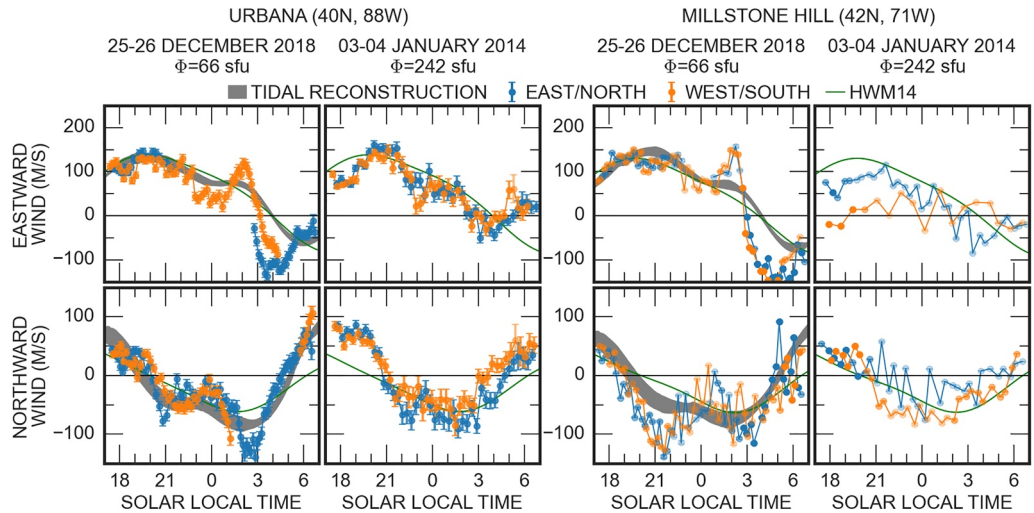

Figure 10. Comparison of zonal (top) and meridional (bottom) thermospheric winds for low (left) and high (right) solar flux conditions during the 25–26 December 2018 over Millstone Hill Fabry-Perot interferometer (FPI) and during the 03–04 January 2014 over Urbana FPI, respectively.

are able to capture the migration to earlier local time for lower latitudes of the southward peak in the post-midnight sector. As shown in this figure, the post-midnight southward peaks in Boulder and Morocco are located at 03:00 and 01:00 SLT, respectively.

5.4. Solar Flux Variations

Our results in Section 5.2.2 indicate strong terdiurnal and quatradiurnal tides for similar low solar flux conditions during late December and early January over the East of Boulder, Urbana and Millstone Hill. For a further analysis of the historical data under different geophysical conditions, Figure 10 compares two nights for low and high solar flux conditions for the Boulder and Millstone Hill FPIs. The left column of each panel shows corresponding observations for the night of the 25–26 December 2018 when daily solar flux was 66 solar flux units. The right column of each panel shows corresponding observations for the night of the 03–04 January 2014 when the daily solar flux was 242 solar flux units. As in previous figures, the green solid lines are predictions from HWM14 and shaded areas in gray are ICON/MIGHTI tidal reconstructions. The 25–26 December 2018 zonal winds for both FPI sites show a similar structure as in previous figures with a strong peak of ∼150 m/s around 02:30 SLT and low westward magnitudes around 05:00 SLT. For the 03–04 January 2014 night, the structure follows a similar trend, but has heavily reduced local time dependence as compared with the left columns on each panel, indicating a suppression of the terdiurnal and higher-order tidal components during high solar flux conditions. This interpretation is consistent with our results of terdiurnal and quatradiurnal tidal origin for the post-midnight eastward wind sector, shown above. Similarly, the Millstone Hill meridional data for low solar flux conditions shows a similar structure of strong decrease of the southward winds around midnight which is consistent with our previous results. This structure is also partly reproduced by our tidal reconstruction and strongly damped in the high solar flux for both FPI observations. Figure 10 shows that for lower solar flux conditions, the terdiurnal and quatradiurnal tides are stronger. These effects were previously recognized in Figures 6 and 7 to be strong in the post- and mid-night sectors for the eastward and northward winds respectively. These effects are particularly strong for the night of 25–26 December 2018 since the daily solar flux was very small.

To understand how common this feature is, Figure 11 compares the zonal and meridional components of the thermospheric winds for different solar flux conditions using the historical database from the ground-based instrumentation. We used two solar flux ranges and show the climatological average values for the two first weeks of January when high-order tidal components are stronger as shown by Figure 3. The top (bottom) panels show the eastward (northward) winds for lower ($\phi < 120$, solid lines) and higher ($120 < \phi < 180$, dashed lines) solar flux conditions relative to East/North of the Boulder (left), Urbana (mid) and Millstone Hill (right) FPIs. The zonal winds shown in this figure are eastward, reach maximum magnitudes around 21:00 SLT, decrease

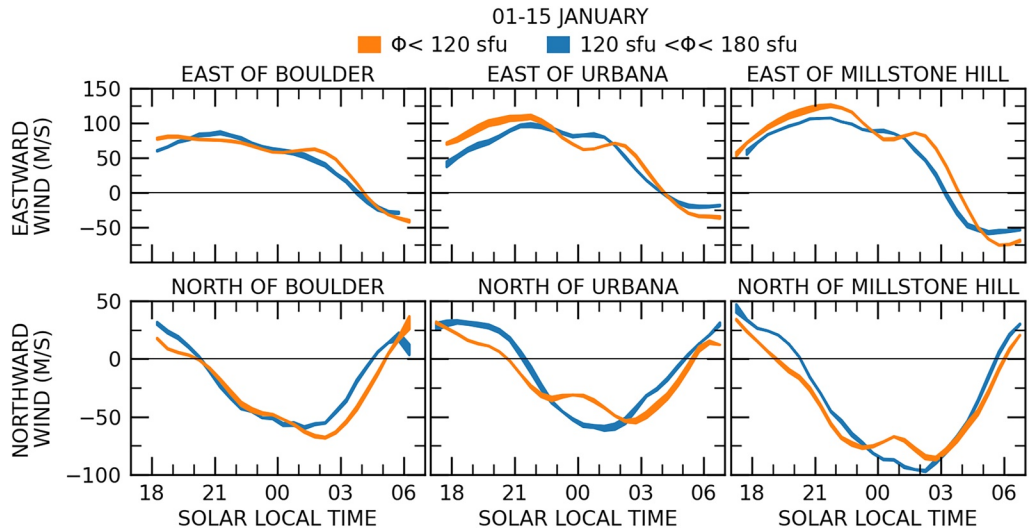

Figure 11. Comparison of climatological averages of thermospheric winds for low (orange) and medium (blue) solar flux activity conditions for the period of 01–15 January over the East (top) and North (bottom) of Boulder (left), Urbana (mid) and Millstone Hill (right) Fabry-Perot interferometer sites.

with a secondary maximum around 02:00 SLT, and reverse around 03:30 SLT for the three sites, except that the maximum magnitudes are about 50 m/s stronger at Millstone Hill and the early morning winds show stronger westward winds of −75 m/s for Millstone Hill. The meridional winds are northward early in the night, decrease and reverse southward around 20:30 (19:00) SLT at Boulder and Urbana (Millstone Hill), reach maximum southward magnitudes at ∼22:00 and ∼03:00 SLT, decrease in magnitude and reverse northward at 06:00 (05:00) SLT at Millstone Hill (Urbana and Boulder). The maximum southward magnitudes are about 75 m/s stronger over Millstone Hill. For higher solar flux conditions, the solar local dependence of both wind components at all sites is similar except for the maximum peak, which seems to be much weaker.

This figure shows that for higher solar flux conditions, the terdiurnal and quatradiurnal tidal signature is weaker. The double-peak structures observed in the lower solar flux eastward and northward wind is consistent with previous results and with effects coming from below which are generally stronger for lower solar flux conditions. These results indicate that terdiurnal and quatradiurnal signatures are due to upward-propagating tidal effects that penetrate more effectively into the thermosphere during solar minimum than during solar maximum. Also, these effects seem to affect the meridional winds first, which is aligned with our results on latitudinal tidal migration previously discussed for Figures 9–11.

These results on tidal origin, together with results on low-latitude migration from the previous section, indicate that the structures in the thermospheric wind are related to a tidal migration along the meridional direction from lower latitudes that becomes stronger for lower solar flux conditions. This suggest that the semidiurnal and terdiurnal tides have a more effective altitudinal penetration from the MLT to the thermospheric region during low solar flux conditions, a well-known behavior of vertically propagating tides (Oberheide et al., 2009). The tidal migration is well aligned with Moudden and Forbes (2013) who showed a seasonal migration of the terdiurnal tides in the MLT region. This migration was, through nonlinear interactions, tied to a migration of the semidiurnal tides along the north-south direction that was strongest in the northern hemisphere around middle of December solstice; this is when our observations also showed stronger terdiurnal and quatradiurnal tidal effects as shown in Section 5.1.

Other studies remark on the role of non-linear interactions in the generation of non-migrating tides. Forbes and Wu (2006) found strong TW2 and TW4 tidal components in the lower MLT region using MLS-UARS temperature observations. Moudden and Forbes (2013) found the dominant nonmigrating terdiurnal tides to be TE1, TW4 and TW5, and attributed their existence to various interactions involving DE3, DW2, DW1 and SW2 and SW4. Jones et al. (2013) showed that ion-neutral coupling was an important source for generating non-migrating tidal components for increasing solar flux conditions during daytime. They indicated that longitudinal structures in the plasma density driven by longitudinal structures in the high-latitude magnetic field configuration and

the longitudinal structures in the neutral wind circulation can non-linearly interact due to the hydromagnetic coupling of the plasma density and the neutral winds. In particular, D0 and DW2 are generated from hydromagnetic coupling between SPW1 tides in the ionospheric plasma and DW1 tides in the neutral wind circulation. Several other semidiurnal tidal components SE1, S0, SW1, and SW3 were also found due to SW2 interactions with SPW3, SPW2, and SPW1, respectively, which is consistent with CHAMP observations from Häusler and Lühr (2009) and Häusler et al. (2010). Likewise, Forbes et al. (2021) attributed the presence of SE2, SPW4, and DW5 in the thermosphere and ionosphere to a series of nonlinear interactions. Maute et al. (2023) also found strong SW2, TW3, and QW4 migrating tides following a Hough Mode Extension tidal analysis of the ICON neutral winds during the August–September 2020 period. They suggested that these TW3 and QW4 tides were non-linearly generated by the interaction of DW1 and SW2 and of SW2 and TW3 respectively. It seems clear that nonlinear interactions involving solar tides are responsible for a degree of complexity in the I-T system that was previously under-appreciated.

These studies noted the importance of semidiurnal tides in the generation of higher order non-migrating tides through non-linear interactions. Our results indicate that longer-period tidal components are reduced for higher solar flux as shown by the pre-midnight eastward winds and that terdiurnal, quatradiurnal and potentially other higher components are stronger for lower solar flux conditions during December solstice and dominant for higher latitudes as shown by the post-midnight eastward winds. The reduction of the semidiurnal and shorter-period tides during higher solar flux conditions at midlatitudes (Häusler et al., 2010; Oberheide et al., 2009) is well aligned with the interpretation of non-linear interaction as generation mechanism and with our results. The seasonal migration of semidiurnal and terdiurnal tides in the lower thermosphere (Moudden & Forbes, 2013) is also well aligned with our results and can potentially be considered a contributing source for these structures.

6. Summary and Conclusions

We examined a large solar local-time structure in F-region neutral winds that has not been recognized in previous observations of the midlatitude thermosphere. This SLT structure was persistently observed during the 2019–2020 December solstice by both ground-based FPIs and the ICON/MIGHTI instrument with the largest effect around late December and early January. The structure exhibited strong eastward winds around 20:00–22:00 SLT and around 02:00 SLT, with minimum magnitudes around midnight, and similar local time effects but weaker magnitudes in the northward winds. A tidal analysis was performed using the ICON/MIGHTI and historical FPI observations with the following results:

1. Tidal analysis of the ICON/MIGHTI zonal wind observations reveals that the signature of this SLT structure in the pre-midnight eastward winds is mostly explained by diurnal and semidiurnal tides, and that the signature in the post-midnight eastward winds can be explained by the terdiurnal and quatradiurnal tidal components. The longitudinal dependence, due to the non-migrating part of the tidal spectrum, shows a dual-peak structure around 200°–120°W and 30°W–60°E for the post-midnight sector.
2. Similarly, tidal analysis for the meridional winds shows a much larger variability in different local time sectors after removing longer-period tidal harmonics. They show northward winds in the midnight sector and southward winds in the post-midnight sector. Their longitudinal dependence also shows a dual peak structure as in the post-midnight eastward winds but with weaker magnitudes.
3. Our ICON/MIGHTI tidal reconstructions using terdiurnal and quatradiurnal tides reproduce the SLT structure observed in the eastward and northward ground-based wind observations. The spectral analysis of the Boulder, Urbana and Millstone Hill FPI data sets during December solstice and for lower solar flux conditions show that the terdiurnal and quatradiurnal tides are strongest around late December and early January. Similarly, our comparisons with Morocco in northern Africa show that the terdiurnal and quatradiurnal tides are also stronger in the post-midnight sector for the eastward winds and in the midnight sector in the northward winds.
4. Our analysis reveals that this structure is mostly explained by D0, DE2, DE1, DW1, DW2, SE2, SE3, SW2, SW4, TE2, TE4, TW3, QW2, and QW6 for the eastward winds and by D0, DE4, DE1, DW1, DW2, DW4, SW3, SW2, SW4, S0, T0, TW2, TW5, TW1, TE1, QW3, QW5 for the northward winds. Our tidal reconstructions at different latitudes show that these structures were stronger for increasing latitudes. Their effects reach further south up to ∼20°N for the post-midnight eastward winds around 180°–120°W and about the same latitudes for the northward midnight winds around 0°–60°E. We find that these longitudinal variations were well aligned with the magnetic declination of Earth's magnetic field. The latitudinal variations are also

well defined by the magnetic inclination. The diurnal and semidiurnal tides are stronger for latitudes below 30°N. The terdiurnal and quatradiurnal magnitudes are strongest for the highest bin available at ∼39°N latitude for both wind components. Their magnitudes were strong up to 30°N and later migrate to earlier local times reaching midnight for 21°N for the eastward winds. Similarly, tidal components of the northward winds migrate to earlier local times from 05:00 to 01:00 SLT in the post-midnight sector. Moreover, this local time migration of the strongest southward peak in the post-midnight sector were also observed in Boulder and Morocco FPIs and in agreement with our tidal reconstructions.

5. Similarly, the latitudinal migration of the terdiurnal and quatradiurnal tidal components is driven along the south-to-north direction by meridional wind tidal components. These tides strengthen the tidal components in the eastward winds for latitudes above 30°N, probably through nonlinear interactions combined with effects of the magnetic inclination of Earth's magnetic field.
6. Climatological averages under lower and higher solar flux conditions show that the structures under study are stronger for lower solar flux conditions and often observed during December solstices. These results indicate a tidal origin of these structures which are generally stronger for lower solar flux conditions. This also suggests a more effective altitudinal penetration of upwardly propagating semidiurnal and/or terdiurnal tidal effects into the thermosphere during solar minimum than during solar maximum.

Our results show, to the best of our knowledge, for the first time the strong non-migrating tidal effects over the midlatitude thermosphere using data sets from different observing platforms. We developed a tidal analysis procedure that enabled much deeper insight into these effects. Modeling studies are needed to better understand the competing roles of different forces of pressure gradient, ion drag, effects coming from below and from higher latitudes to further understand the midlatitude thermospheric dynamics during December solstice as revealed by our results.

Appendix A: Aliasing Analysis

Section 4 of this manuscript refers to Moudden and Forbes (2013) regarding the potential aliasing between tidal components with the same zonal wavenumbers. This relates to the diurnal and semidiurnal tides affecting the magnitudes of the terdiurnal and quadradiurnal tidal components when performing the tidal analysis. However, as Moudden and Forbes (2013) show, these effects are greatly reduced by removing the longer tidal components and performing the tidal analysis over the resulting residuals. Our methodology follows that of Moudden and Forbes (2013), except we also select the strongest tidal components. We performed a synthetic data analysis to assess the aliasing effects of longer-period tidal components into shorter-period tidal magnitudes of the same wavenumber.

In our aliasing analysis, the input field has the same spatial and temporal distribution as ICON/MIGHTI observations, but the value of the winds is set to match a synthetic wind field obtained from a chosen tidal population. The tidal population was chosen to assess the potential aliasing of diurnal and semidiurnal tidal components into terdiurnal and quadradiurnal tidal components. We first evaluate the potential aliasing when considering only diurnal and semidiurnal tides for the input wind field. Figure A1 shows the analysis of an input tidal spectrum considering only diurnal and terdiurnal tides. The top row shows the tides magnitudes of the diurnal and semidiurnal spectra set up to a fixed magnitude of 5 m/s. All other tidal magnitudes and phases were set to zero. The bottom row shows the output tide magnitudes for each tidal component and latitudinal bin. The tide magnitudes after following our methodology are mostly contained within the diurnal and semidiurnal spectra with strongest magnitudes of ∼0.5 m/s for TW2 and TW3 at lower latitudes. Note that the diurnal and semidiurnal tidal magnitudes were stronger for decreasing latitudes and for lower wavenumbers (e.g., from DE3 to DW3).

Our analysis from Figures 3 and 4 suggested the potential for aliasing from wavenumbers between DE2 to DW2, and from SE3 to SW3 into terdiurnal and quadradiurnal tides. Figure A2 considers the synthetic case of all tidal magnitudes fixed to 5 m/s. As for our previous synthetic case, the resultant tidal magnitudes show very little aliasing effect, and their magnitudes decrease for increasing zonal wavenumbers. Similarly, the tidal magnitudes are stronger for decreasing latitudes and smaller zonal wavenumbers for diurnal, semidiurnal, terdiurnal and quadradiurnal tides. They reached maximum from DE1 to DW1, SE1 to SW1, TE1 to TW1 and QW1 to QE1 with magnitudes of 5.5, 6, 5.8, 5.3 m/s respectively. Our intermediate plots showed that the increasing magnitudes are related to the lack of observations, due to the South Atlantic Anomaly (SAA), rather

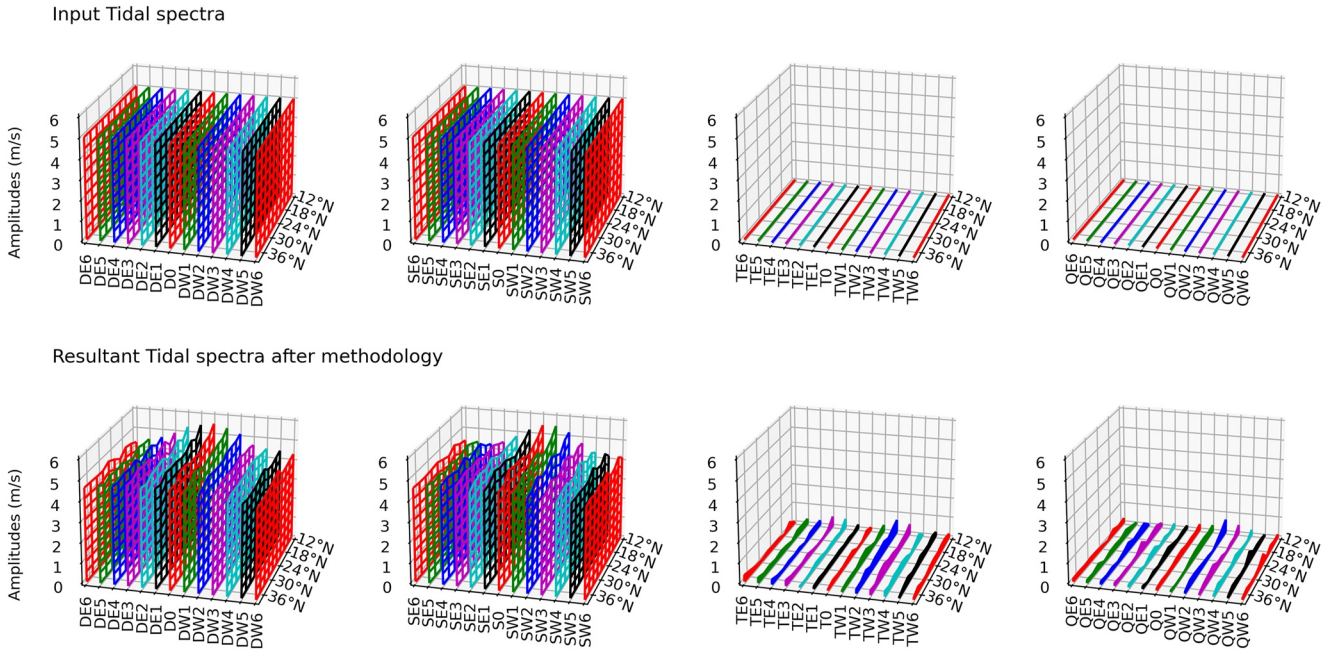

Figure A1. (Top) Synthetic tidal spectra considering only diurnal and semidiurnal tides with a fixed amplitude of 5 m/s at each latitudinal bin. (Bottom) Resultant tidal spectra following our methodology.

than aliasing effects. This increment for the wavenumbers is of 1 m/s for the lowest latitudinal bin of 12°N. We conclude this effect is less than 10% over the original wind field and does not affect our results for smaller zonal wavenumbers, and the main reason of the latitudinal bin of 12°N was chosen as lower latitudinal limit for Figure 7.

To further evaluate the effect of the SAA into the resultant tidal magnitudes, we consider the same tidal spectra of all tidal magnitudes fixed to a single amplitude as in Figure A2 but extended the latitudinal bins

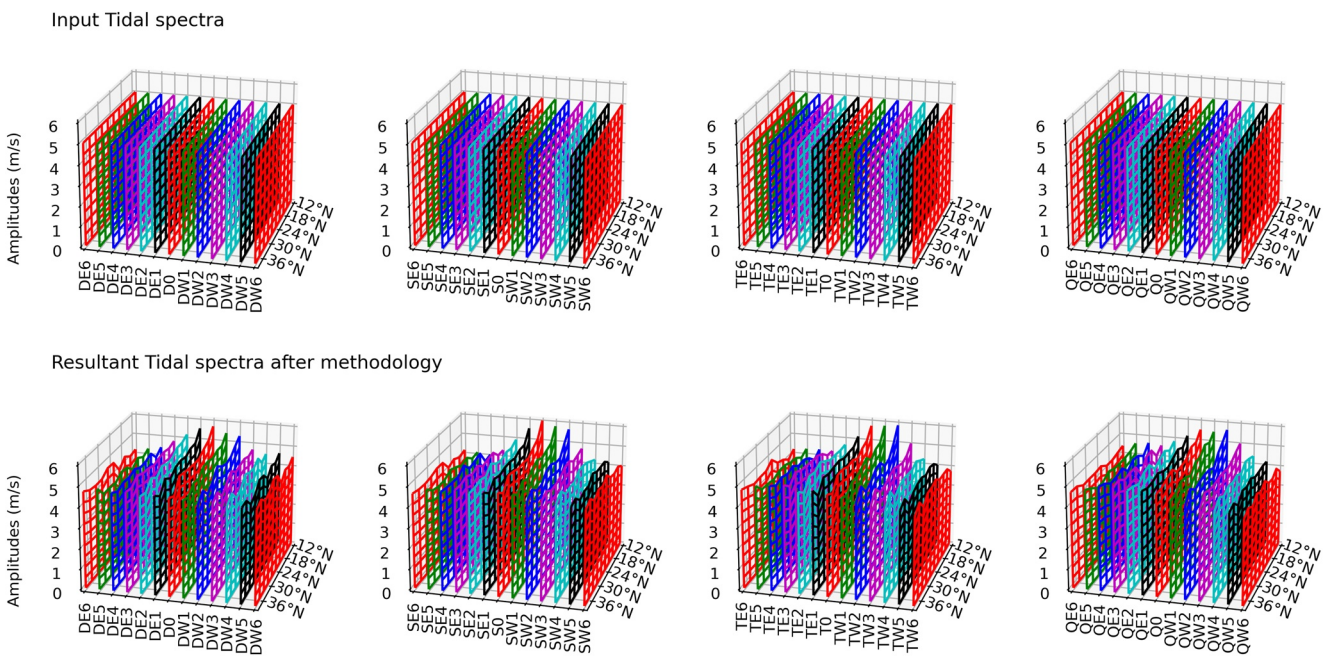

Figure A2. Same as Figure A1 except that input spectra of terdiurnal and quadradiurnal tides are also set to a fixed magnitude of 5 m/s.

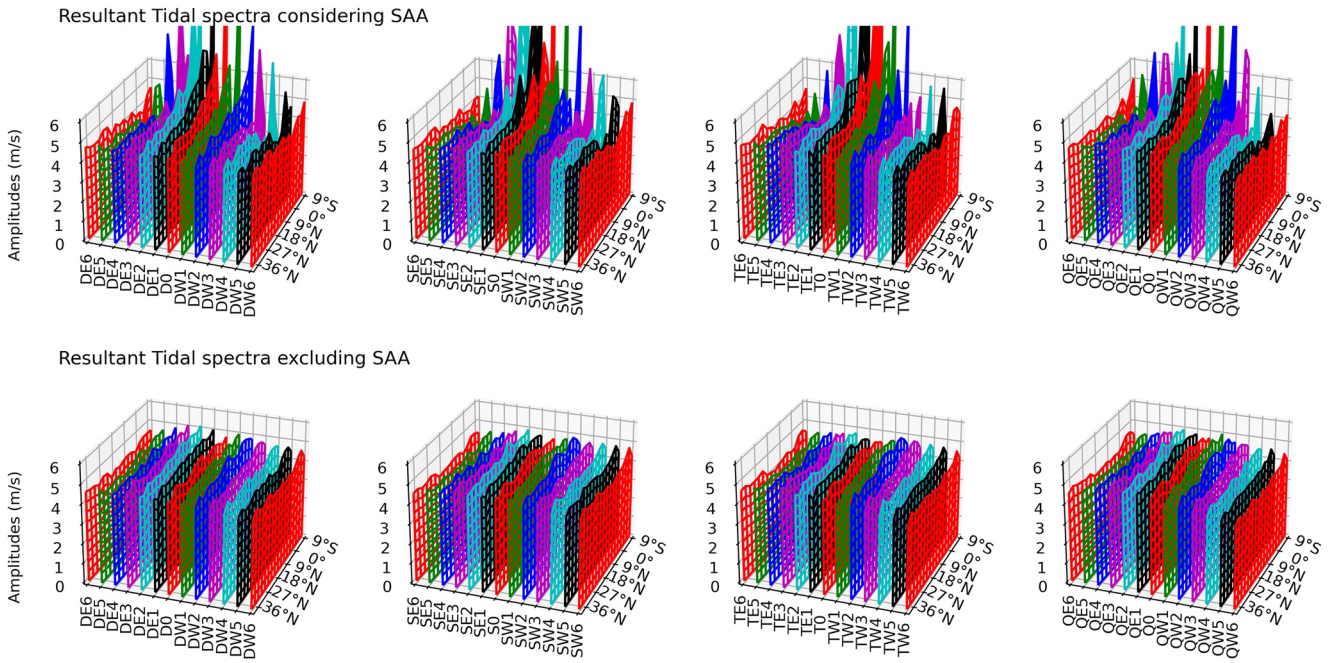

Figure A3. (Top) Resultant tidal spectra following our methodology considering same synthetic tidal amplitudes as in Figure A2 except that latitudinal bins are extended up to 9°S. (Bottom) Resultant tidal spectra following our methodology but filling the longitudinal gap due to the South Atlantic Anomaly with wind field population from midlatitude bins.

up to 9°S to observe strongest effects due to the SAA. Also, we used the wind field population around the SAA longitudinal sector (e.g., 245°E–355°E) of the highest latitudinal bin (i.e., 33°N–39°N which shows no SAA effects) to fill in the gap at other latitudinal bins as the SAA effect grows stronger for decreasing latitudes. Figure A3 shows the results from this setup. The top row shows the same resultant tidal spectra as in Figure A2 except that it also shows results for lower latitudinal bins up to 9°S. The bottom row shows the resultant tidal spectra when excluding the SAA by matching the wind field population of latitudinal bins at midlatitudes that are not affected by the SAA. We conclude that SAA is certainly an important limitation for our procedure. Nevertheless, as stated above, the zonal wavenumbers affected by the SAA has an effect of less than 10% of the true tidal magnitude within the latitudinal bins considered in this study, that is, higher than 12°N. We conclude that aliasing and SAA effects are greatly reduced by our methodology and do not affect our results.

Acknowledgments
ICON is supported by NASA's Explorer Program through contracts NNG12FA45C and NNG12FA42I. This work was partly supported by National Science Foundation CEDAR Grant AGS 2230438 to the University of Colorado. Operation of the FPIs is supported at the University of Illinois Urbana-Champaign by National Science Foundation CEDAR Grant AGS 1932953. Deployment of the FPI instrumentation to Morocco, was supported by National Science Foundation CEDAR Grants AGS 1138998 and AGS 1452291 as well as by NASA Grant NNX14AD46G. FPI measurements and operations at Boulder are supported by NSF Grant AGS 2120511 and by NASA LWS Grant 80NSSC20K0199, NASA GIGI Grant 80NSSC22K0170 and NASA Grant 80NAAC21K0014 to the University Corporation for Atmospheric Research. The CPI work on the data used is supported by NSF Grant AGS 2030679.

Data Availability Statement

ICON data are processed in the ICON Science Data center at UCB and available at https://icon.ssl.berkeley.edu/Data. The FPI data are available through the CEDAR Madrigal database (http://cedar.openmadrigal.org/openmadrigal/) and NCAR database (https://fpi.hao.ucar.edu/).

References

Alken, P. (2009). A quiet time empirical model of equatorial vertical plasma drift in the Peruvian sector based on 150 km echoes. *Journal of Geophysical Research*, *114*(A2), A02308. https://doi.org/10.1029/2008JA013751

Brum, C. G. M., Tepley, C. A., Fentzke, J. T., Robles, E., dos Santos, P. T., & Gonzalez, S. A. (2012). Long-term changes in the thermospheric neutral winds over Arecibo: Climatology based on over three decades of Fabry-Perot observations. *Journal of Geophysical Research*, *117*(A2), A00H14. https://doi.org/10.1029/2011JA016458

Chu, K. (2019). Tidal analysis of modeled thermospheric winds to improve agreement with measurements over South Africa Master's thesis. University of Illinois Urbana-Champaign. Retrieved from http://hdl.handle.net/2142/104808

Crary, D. J., & Forbes, J. M. (1986). The dynamic ionosphere over Arecibo: A theoretical investigation. *Journal of Geophysical Research*, *91*(A1), 249–258. https://doi.org/10.1029/JA091iA01p00249

Cullens, C. Y., Immel, T. J., Triplett, C. C., Wu, Y.-J., England, S. L., Forbes, J. M., & Liu, G. (2020). Sensitivity study for ICON tidal analysis. *Progress in Earth and Planetary Science*, *7*(1), 18. https://doi.org/10.1186/s40645-020-00330-6

Dandenault, P. B., & Richards, P. G. (2015). The collapse of the mid- night ionosphere and behavior of meridional neutral winds at Townsville over a full solar cycle. *Journal of Geophysical Research: Space Physics*, *120*(11), 9826–9838. https://doi.org/10.1002/2015JA021842

Drob, D. P., Emmert, J. T., Meriwether, J. W., Makela, J. J., Doornbos, E., Conde, M., et al. (2015). An update to the Horizontal Wind Model (HWM): The quiet time thermosphere. *Earth and Space Science*, *2*(7), 301–319. https://doi.org/10.1002/2014EA000089

Emmert, J. T., Fejer, B. G., & Sipler, D. P. (2003). Climatology and latitudinal gradients of quiet time thermospheric neutral winds over Millstone Hill from Fabry-Perot interferometer measurements. *Journal of Geophysical Research*, *108*(A5), 1196. https://doi.org/10.1029/2002JA009765

Englert, C. R., Harlander, J. M., Brown, C. M., Marr, K. D., Miller, I. J., Stump, J. E., et al. (2017). Michelson interferometer for global high-resolution thermospheric imaging (MIGHTI): Instrument design and calibration. *Space Science Reviews*, *212*(1), 553–584. https://doi.org/10.1007/s11214-017-0358-4

Englert, C. R., Harlander, J. M., Marr, K. D., Harding, B. J., Makela, J. J., Fae, T., et al. (2023). Michelson interferometer for global high-resolution thermospheric imaging (MIGHTI) on-orbit wind observations: Data analysis and instrument performance. *Space Science Reviews*, *219*(3), 27. https://doi.org/10.1007/s11214-023-00971-1

Faivre, M., Meriwether, J. W., Fesen, C. G., & Biondi, M. A. (2006). Climatology of the midnight temperature maximum phenomenon at Arequipa, Peru. *Journal of Geophysical Research*, *111*(A6), A06302. https://doi.org/10.1029/2005JA011321

Fisher, D. J., Makela, J. J., Meriwether, J. W., Buriti, R. A., Benkhaldoun, Z., Kaab, M., & Lagheryeb, A. (2015). Climatologies of nighttime thermospheric winds and temperatures from Fabry-Perot interferometer measurements: From solar minimum to solar maximum. *Journal of Geophysical Research: Space Physics*, *120*(8), 6679–6693. https://doi.org/10.1002/2015JA021170

Forbes, J. M. (1982). Atmospheric tides: 1. Model description and results for the solar diurnal component. *Journal of Geophysical Research*, *87*(A7), 5222–5240. https://doi.org/10.1029/ja087ia07p05222

Forbes, J. M. (1995). Tidal and planetary waves. In *The upper mesosphere and lower thermosphere: A review of experiment and theory* (pp.67–87). American Geophysical Union (AGU). https://doi.org/10.1029/GM087p0067

Forbes, J. M. (2021). Atmosphere-ionosphere (A-I) coupling by solar and lunar tides. In W. Wang, Y. Zhang, & L. J. Paxton, (Ed.), *Space physics and aeronomy, volume 4, upper atmosphere dynamics and energetics* (pp.159–182). American Geophysical Union 560. https://doi.org/10.1002/9781119815631.ch9

Forbes, J. M., & Wu, D. (2006). Solar tides as revealed by measurements of mesosphere temperature by the MLS experiment on UARS. *Journal of the Atmospheric Sciences*, *63*(7), 1776–1797. https://doi.org/10.1175/JAS3724.1

Forbes, J. M., Zhang, X., Heelis, R., Stoneback, R., Englert, C. R., Harlan- der, J. M., et al. (2021). Atmosphere-ionosphere (A-I) coupling as viewed by ICON: Day-to-day variability due to planetary wave (PW)-Tide interactions. *Journal of Geophysical Research: Space Physics*, *126*(6), e2020JA028927. https://doi.org/10.1029/2020JA028927

Forbes, J. M., Zhang, X., Palo, S., Russell, J., Mertens, C. J., & Mlynczak, M. (2008). Tidal variability in the ionospheric dynamo region. *Journal of Geophysical Research*, *113*(A2), A02310. https://doi.org/10.1029/2007JA012737

Forbes, J. M., Zhang, X., Talaat, E. R., & Ward, W. (2003). Nonmigrating diurnal tides in the thermosphere. *Journal of Geophysical Research*, *108*(A1), 1033. https://doi.org/10.1029/2002JA009262

Hagan, M. E., Maute, A., & Roble, R. G. (2009). Tropospheric tidal effects on the middle and upper atmosphere. *Journal of Geophysical Research*, *114*(A1), A01302. https://doi.org/10.1029/2008JA013637

Harding, B. J., Gehrels, T. W., & Makela, J. J. (2014). Nonlinear regression method for estimating neutral wind and temperature from Fabry-Perot interferometer data. *Applied Optics*, *53*(4), 666–673. https://doi.org/10.1364/AO.53.000666

Harding, B. J., Makela, J. J., Englert, C. R., Marr, K. D., Harlander, J. M., England, S. L., & Immel, T. J. (2017). The MIGHTI wind retrieval algorithm: Description and verification. *Space Science Reviews*, *212*(1), 585–600. https://doi.org/10.1007/s11214-017-0359-3

Häusler, K., & Lühr, H. (2009). Nonmigrating tidal signals in the upper thermospheric zonal wind at equatorial latitudes as observed by CHAMP. *Annales Geophysicae*, *27*(7), 2643–2652. https://doi.org/10.5194/angeo-27-2643-2009

Häusler, K., Lühr, H., Hagan, M. E., Maute, A., & Roble, R. G. (2010). Comparison of CHAMP and TIME-GCM nonmigrating tidal signals in the thermospheric zonal wind. *Journal of Geophysical Research*, *115*(D1), D00I08. https://doi.org/10.1029/2009JD012394

Herrero, F., & Meriwether, J. (1980). 6300-Å airglow meridional intensity gradients. *Journal of Geophysical Research*, *85*(A8), 4191–4204. https://doi.org/10.1029/JA085iA08p04191

Hickey, D. A., Martinis, C. R., Erickson, P. J., Goncharenko, L. P., Meriwether, J. W., Mesquita, R., et al. (2014). New radar observations of temporal and spatial dynamics of the midnight temperature maximum at low latitude and midlatitude. *Journal of Geophysical Research: Space Physics*, *119*(12), 10499–10506. https://doi.org/10.1002/2014JA020719

Immel, T. J., England, S. L., Mende, S. B., Heelis, R. A., Englert, C. R., Edelstein, J., et al. (2018). The ionospheric connection explorer mission: Mission goals and design. *Space Science Reviews*, *214*(1), 13. https://doi.org/10.1007/s11214-017-0449-2

Jones, M., Jr., Forbes, J. M., Hagan, M. E., & Maute, A. (2013). Non-migrating tides in the ionosphere-thermosphere: In situ versus tropospheric sources. *Journal of Geophysical Research: Space Physics*, *118*(5), 2438–2451. https://doi.org/10.1002/jgra.50257

Kato, S. (Ed.) (1980). *Dynamics of the upper atmosphere*. Springer Netherlands.

Lühr, H., & Manoj, C. (2013). The complete spectrum of the equatorial electrojet related to solar tides: CHAMP observations. *Annales Geophysicae*, *31*(8), 1315–1331. https://doi.org/10.5194/angeo-31-1315-2013

Makela, J. J., Baughman, M., Navarro, L. A., Harding, B. J., Englert, C. R., Harlander, J. M., et al. (2021). Validation of ICON-MIGHTI thermospheric wind observations: 1. Nighttime red-line ground-based Fabry-Perot interferometers. *Journal of Geophysical Research: Space Physics*, *126*(2), e2020JA028726. https://doi.org/10.1029/2020JA028726

Makela, J. J., Fisher, D. J., Meriwether, J. W., Buriti, R. A., & Medeiros, A. F. (2013). Near-continual ground-based nighttime observations of thermospheric neutral winds and temperatures over equatorial Brazil from 2009 to 2012. *Journal of Atmospheric and Solar-Terrestrial Physics*, *103*, 94–102. https://doi.org/10.1016/j.jastp.2012.11.019

Makela, J. J., Meriwether, J. W., Ridley, A. J., Ciocca, M., & Castellez, M. W. (2012). Large-scale measurements of thermospheric dynamics with a multisite Fabry-Perot interferometer network: Overview of plans and results from midlatitude measurements. *International Journal of Geophysics*, *2012*, 1–10. https://doi.org/10.1155/2012/872140

Martinis, C., Hickey, D., Oliver, W., Aponte, N., Brum, C. G. M., Akmaev, R., et al. (2013). The midnight temperature maximum from Arecibo incoherent scatter radar ion temperature measurements. *Journal of Atmospheric and Solar-Terrestrial Physics*, *103*, 129–137. https://doi.org/10.1016/j.jastp.2013.04.014

Maute, A., Forbes, J. M., Cullens, C. Y., & Immel, T. J. (2023). Delineating the effect of upward propagating migrating solar tides with the TIEGCM-ICON. *Frontiers in Astronomy and Space Sciences*, *10*, 1147571. https://doi.org/10.3389/fspas.2023.1147571

Meriwether, J., Faivre, M., Fesen, C., Sherwood, P., & Veliz, O. (2008). New results on equatorial thermospheric winds and the midnight temperature maximum. *Annales Geophysicae*, *26*(3), 447–466. https://doi.org/10.5194/angeo-26-447-2008

Mesquita, R. L. A., Meriwether, J. W., Makela, J. J., Fisher, D. J., Harding, B. J., Sanders, S. C., et al. (2018). New results on the mid-latitude midnight temperature maximum. *Annales Geophysicae*, *36*(2), 541–553. https://doi.org/10.5194/angeo-36-541-2018

Moudden, Y., & Forbes, J. M. (2013). A decade-long climatology of terdiurnal tides using TIMED/SABER observations. *Journal of Geophysical Research: Space Physics*, *118*(7), 4534–4550. https://doi.org/10.1002/jgra.50273

Nelson, G. J., & Cogger, L. L. (1971). Dynamical behaviour of the nighttime ionosphere at Arecibo. *Journal of Atmospheric and Terrestrial Physics*, *33*(11), 1711–1726. https://doi.org/10.1016/0021-9169(71)90219-4

Oberheide, J., Forbes, J. M., Ha¨usler, K., Wu, Q., & Bruinsma, S. L. (2009). Tropospheric tides from 80 to 400 km: Propagation, interannual variability, and solar cycle effects. *Journal of Geophysical Research*, *114*, D00I05. https://doi.org/10.1029/2009JD012388

Ojo, T. T., Katamzi-Joseph, Z. T., Chu, K. T., Grawe, M. A., & Makela, J. J. (2022). A climatology of the nighttime thermospheric winds over Sutherland, South Africa. *Advances in Space Research*, *69*(1), 209–219. https://doi.org/10.1016/j.asr.2021.10.015

Richmond, A. D. (1983). Thermospheric dynamics and electrodynamics. In R. L. Carovillano, & J. M. Forbes (Eds.), *Solar-terrestrial physics* (pp. 523–607).

Teitelbaum, H., & Vial, F. (1991). On tidal variability induced by nonlinear interaction with planetary waves. *Journal of Geophysical Research*, *96*(A8), 14169–14178. https://doi.org/10.1029/91JA01019

Truskowski, A. O., Forbes, J. M., Zhang, X., & Palo, S. E. (2014). New perspectives on thermosphere tides: 1. Lower thermosphere spectra and seasonal-latitudinal structures. *Earth Planets and Space*, *66*(1), 136. https://doi.org/10.1186/s40623-014-0136-4

Wu, Q., Gablehouse, R. D., Solomon, S. C., Killeen, T. L., & She, C.-Y. (2004). A new Fabry-Perot interferometer for upper atmosphere research, Proc. SPIE 5660, Instruments, Science. *Methods for Geospace and Planetary Remote Sensing*, *218*. https://doi.org/10.1117/12.573084

Zhang, X., Forbes, J. M., & Hagan, M. E. (2010a). Longitudinal variation of tides in the MLT region: 1. Tides driven by tropospheric net radiative heating. *Journal of Geophysical Research*, *115*(A6), A06316. https://doi.org/10.1029/2009JA014897

Zhang, X., Forbes, J. M., & Hagan, M. E. (2010b). Longitudinal variation of tides in the MLT region: 2. Relative effects of solar radiative and latent heating. *Journal of Geophysical Research*, *115*(A6), A06317. https://doi.org/10.1029/2009JA014898